chemosensors

MDPI

Article

Influence of pH on Room-Temperature Synthesis of Zinc Oxide Nanoparticles for Flexible Gas Sensor Applications

Fazia Mechai [1,2,3], Ahmad Al Shboul [1,*], Mohand Outahar Bensidhoum [2,3], Hossein Anabestani [4], Mohsen Ketabi [1] and Ricardo Izquierdo [1,*]

[1] Department of Electrical Engineering, École de Technologie Supérieure (ETS), 1100 Notre-Dame St W, Montreal, QC H3C 1K3, Canada; fazia.mechai.1@ens.etsmtl.ca (F.M.); mohsen.ketabi.1@ens.etsmtl.ca (M.K.)
[2] Artificial Vision and Automatic Systems (LVAAS) Laboratory, Mouloud Mammeri University of Tizi-Ouzou (UMMTO), Tizi Ouzou 15000, Algeria; mohand-outahar.bensidhoum@ummto.dz
[3] Faculty of Electrical and Computer Engineering, Mouloud Mammeri University Tizi-Ouzou (UMMTO), Tizi Ouzou 15000, Algeria
[4] Department of Electrical Engineering, McGill University, 845 Sherbrooke St W, Montreal, QC H3A 0G4, Canada; hossein.anabestani@mail.mcgill.ca
* Correspondence: ahmad.al-shboul@etsmtl.ca (A.A.S.); ricardo.izquierdo@etsmtl.ca (R.I.)

Abstract: This research contributes to work on synthesizing zinc oxide nanoparticles (ZnO NPs) at room temperature (RT) and their utilization in flexible gas sensors. RT ZnO NP synthesis with a basicity solution (pH $\approx$ 13) demonstrates an efficient method for synthesizing well-crystalline ZnO NPs (RT.pH13) comparable to those synthesized by the hydrothermal method (hyd.C). The RT.pH13 achieved a high thermal stability with minimal organic reside impurities (~4.2 wt%), 30–80 nm particle size distribution, and a specific surface area (14 m^2 g^{-1}). The synthesized pre- and post-calcinated RT.pH13 NPs were then incorporated into flexible sensors for gas sensing applications at ambient conditions (RT and relative humidity of 30–50%). The pre-calcinated ZnO-based sensor (RT.pH13) demonstrated superior sensitivity to styrene and acetic acid and lower sensitivity to dimethyl-6-octenal. The calcinated ZnO-based sensor (RT.pH13.C) exhibited lower sensitivity to styrene and acetic acid, but heightened sensitivity to benzene, acetone, and ethanol. This suggests a correlation between sensitivity and structural transformations following calcination. The investigation of the sensing mechanisms highlighted the role of surface properties in the sensors' affinity for specific gas molecules and temperature and humidity variations. The study further explored the sensors' mechanical flexibility, which is crucial for flexible Internet of Things (IoT) applications.

Keywords: flexible; gas sensor; room-temperature synthesis; pH effect; printed; zinc oxide

Citation: Mechai, F.; Al Shboul, A.; Bensidhoum, M.O.; Anabestani, H.; Ketabi, M.; Izquierdo, R. Influence of pH on Room-Temperature Synthesis of Zinc Oxide Nanoparticles for Flexible Gas Sensor Applications. *Chemosensors* **2024**, *12*, 83. https://doi.org/10.3390/chemosensors12050083

Received: 31 March 2024
Revised: 3 May 2024
Accepted: 7 May 2024
Published: 16 May 2024

1. Introduction

Zinc oxide nanomaterials (ZnO NMs) have garnered significant attention as one of the most extensively studied metal oxides for diverse applications [1,2], particularly in chemical sensing [3]. This interest stems from their inherent advantages, including high sensitivity, stability, and cost-effectiveness [2]. ZnO falls under group II-VI semiconductors in materials [4]. With a wide bandgap of 3.0–3.37 eV [3,5], ZnO exhibits visible light and near UV radiation transparency [6], rendering it ideal for optical sensing applications [7]. Notably, ZnO nanoparticles (NPs) boast a surface area of 10–100 m^2 g^{-1} [8,9], which is advantageous in gas sensing applications [10,11]. The high surface area facilitates many active sites available for gas adsorption, thereby enhancing sensitivity.

ZnO further distinguishes itself with its high chemical, thermal, and mechanical stability at room temperature (RT) [12,13], making it well suited for deployment in challenging industrial environments [12]. Additionally, ZnO demonstrates enhanced electron mobility, a quality that lends itself to developing sensor devices characterized by rapid response,

stability, and reliability [14,15]. Finally, the distinctive surface chemistry of ZnO positions it as a versatile and favored material for chemical sensing applications [10].

Despite their widespread use, ZnO-based sensors encounter challenges requiring attention for their effective deployment in chemical sensing. Table S1 gives a literature overview of recent ZnO-based sensors. They typically demand high working temperatures (above 100 °C) for optimal sensitivity and selectivity [16], and may exhibit inferior sensing performance at low operating temperatures. Elevated operating temperatures have been an obstacle to the extensive application of ZnO-based gas sensors and hinder the development of flexible sensors on plastic substrates that cannot withstand such heat [17,18]. This limitation hinders their integration into wearable devices and electronics with temperature-sensitive components. In addition, the safety concerns associated with high operating temperatures, particularly in environments with flammable or explosive gases, are of paramount importance. Furthermore, these sensors require extra energy to maintain high operating temperatures, resulting in a higher power consumption and potentially shorter battery life in portable devices.

Additionally, the humidity sensitivity of ZnO-based gas sensors is a matter of concern [19]. The long-term stability of ZnO-based gas sensors at higher temperatures or high humidity levels is often compromised, given the gradual degradation of the ZnO film over time [20]. Such limitations can result in inaccuracies, potentially resulting in false positives or negatives in gas sensing applications. Consequently, there is a growing demand for developing RT operational sensors to address the abovementioned limitations as a safer and more practical solution for many modern applications [17,19]. Strategies to address these limitations include using noble metals, carbon-based materials, polymer doping, and composite materials to enhance low-temperature sensing performance [19].

Besides the high operating temperature challenge, the current research progress on ZnO-based gas sensors further aims to address key limitations, such as poor selectivity and lack of stability. Researchers have focused on innovative strategies involving material engineering, surface modification, and sensing mechanism studies to optimize its gas sensing performance (sensitivity, selectivity, and response/recovery time) and long-term stability towards target gases [21]. Innovative strategies have been investigated, like developing 3D hierarchical architectures [22,23], doping [24–26], and UV light irradiation [27]. There is also a growing interest in exploring flexible and wearable sensor designs for practical applications [28]. Researchers have investigated the gas sensing mechanisms of ZnO, focusing on factors like surface adsorption, charge carrier concentration, and catalytic oxidation reactions [29–31]. These advancements are paving the way for a new generation of gas detection technology with the potential to revolutionize safety monitoring, healthcare diagnostics, and industrial process control.

The recent research on ZnO-based gas sensors has primarily focused on the detection gases of carbon monoxide (CO) [32], carbon dioxide (CO_2) [33], hydrogen sulfide (H_2S) [21], nitrogen dioxide (NO_2) [21,34], and ammonia (NH_3) [25,35,36]. The focus on these gases is likely due to their importance in various industrial and environmental applications, where detecting toxic, flammable, or greenhouse gases is crucial for safety.

Alternately, the synthesis of ZnO NMs is challenged by costly procedures, often involving multistep, high-temperature processes, the need for specialized equipment, precise control over reaction conditions, and lengthy processing times. Moreover, these methods may involve harsh reaction conditions and potentially hazardous chemicals. Table S2 concisely summarizes the recent preparation procedure employed for synthesizing ZnO NMs. Various methods can be employed for ZnO synthesis, including vapor deposition [37], hydrothermal synthesis [38], sol-gel [38], biosynthesis [39], the polyol chemistry process [40], and mechanochemical processes [12]. The sol-gel method is a straightforward approach that allows control over particle size and morphology through systematically monitoring reaction parameters [41]. In this method, zinc acetate ($Zn(CH_3COO)_2$) is dissolved in a solvent, and a base is added to initiate hydrolysis. The resulting gel is then dried and calcined at high temperatures of 350–700 °C for 2–4 h [42,43], obtaining ZnONMs with a particle

size range of 20–200 nm [43,44]. Hydrothermal processing involves heating a substrate mixture in an autoclave to a temperature of 100–300 °C and allowing it to sit for several days, producing high-quality ZnO NPs with a narrow size distribution with a particle size range of 25–35 nm [45]. Such methods are often associated with inherent complexities, including the need for specialized equipment, precise control over reaction conditions, and lengthy processing times. Biosynthesis methods represent an eco-friendly and cost-effective alternative, avoiding toxic chemicals by incorporating plant extracts, such as Azadirachta Indica (Neem) or Aloe vera, as essential elements in the synthesis process [46–48]. The plant extract is mixed with zinc salt, and the resulting mixture is heated and stirred to obtain ZnO NPs with a particle size range of 11 nm–618 µm [46–48]. However, this method requires screening microbes and plant extracts, which can be time-consuming [49]. Polyol chemistry is a simple and low-cost method that can yield ZnO NPs with a narrow size distribution with a particle size range of 10–100 nm [40,50]. It involves using a polyol, such as ethylene glycol, as a solvent and reducing agent. $Zn(CH_3COO)_2$ is dissolved in the polyol, and the mixture is heated to obtain ZnO NPs. Nevertheless, challenges arise as a reducing agent can affect the purity of the ZnO NPs [51,52]. Vapor phase synthesis is another method involving a vapor phase reaction to synthesize high-quality ZnO NPs with a narrow size distribution with a particle size range of 10–118 nm [53,54]. Zinc vapor is generated by heating a zinc source, and the vapor is then reacted with an oxygen-containing gas to form ZnO NPs. However, this method requires a high temperature and pressure, making it expensive and time-consuming [53,55].

Advancements in ZnO NMs' synthesis methods have prioritized enhancing eco-friendliness, cost-effectiveness, and the quality of the resulting NMs [43,56]. Consequently, these developments have explored strategies for synthesizing ZnO NPs at RT [57,58]. The RT synthesis approach offers several advantages: simplicity, scalability, and reduced environmental impact. This method presents a promising avenue for streamlining the synthesis process while minimizing resource requirements and operational costs by leveraging ambient conditions and straightforward reaction setups. Additionally, the RT synthesis approach holds the potential for facilitating the large-scale production of ZnO NPs, thereby addressing scalability challenges often encountered with conventional methods.

Recently, investigations have delved into the critical interplay between the solution pH and the physicochemical properties of the synthesized ZnO NPs [59–61]. pH has been found to play a crucial role in determining the properties and behavior of ZnO NPs, such as crystallite sizes [62–64], morphology [62,63,65], optical properties [63,64,66], magnetic behavior [66], and chemical stability [67]. Therefore, understanding the influence of pH is essential for optimizing the performance of ZnO NPs in various applications. It has the potential to revolutionize the entire field of nanomaterial synthesis. Researchers can apply these insights to engineer other nanomaterials with tailored properties for diverse applications by revealing the fundamental principles that govern ZnO NP formation based on pH.

The motivation for our study is to investigate the feasibility of an RT synthesis approach for ZnO NP production through the bath sonication of $Zn(CH_3COO)_2$ salt for 2 h, aiming to provide a practical and sustainable alternative to conventional methods. Additionally, we explore how variations in pH ranging from a neutral (pH $\approx$ 7) to high basicity solution (pH $\approx$ 13) influence the properties of ZnO NPs. Understanding this relationship is crucial for fine-tuning ZnO NPs' physiochemical properties and performance, enhancing stability, and addressing specific challenges in gas sensing applications. This level of control goes beyond just application optimization: it unlocks the door to interpreting the fundamental mechanisms governing ZnO NPs formation. We also compared ZnO NMs' properties before and after calcination at 500 °C for 2 h in the air environment. This comparison extends to ZnO NMs synthesized using hydrothermal methods and under the previously mentioned conditions. Finally, we used ZnO NMs synthesized at RT under an optimized pH level to fabricate flexible gas sensors. We investigated their sensing applications to diverse gases under ambient operational conditions (RT and moderate relative humidity (RH)~30–40%) and compared their performance based on ZnO NMs pre and post the

calcination step at 500 °C for 2 h. The sensor's temperature, RH, and mechanical flexibility performance were also investigated.

2. Materials and Methods

2.1. Materials and Methods

$Zn(CH_3COO)_2$ salt, zinc nitrite ($ZnNO_2$), hexamethylenetetramine (HMTA, $C_6H_{12}N_4$), methanol (MeOH), and sodium hydroxide (NaOH) were sourced from Sigma-Aldrich (St. Louis, MO, USA). We prepared all the solutions with deionized nanopure water (DI) with a resistivity of >18 MΩ cm^{-1}. Graphite (Gt) flake powder (<20 µm flake size), polystyrene (PS, Mw = 154,000 g mol^{-1}), and xylene solvent ACS were obtained from Sigma-Aldrich, St. Louis, MO, USA.

2.2. Hydrothermal Synthesis of ZnO NMs (hyd.C)

ZnO was synthesized via the conventional hydrothermal method described in the literature [68,69]. Briefly, 5 g of $ZnNO_2$ salt and 2 g of HMTA were dissolved in 80 mL of deionized water within an autoclave reactor and then heated at 90 °C for 6 h. Following filtration, the precipitate was washed with deionized water twice and MeOH several times before air-drying overnight. The resultant white colloidal precipitate underwent calcination at 500 °C for 2 h in an air environment to yield the ZnO NMs. The final ZnO was labeled (hyd.C), denoting hydrothermal synthesis and calcination.

2.3. RT Synthesis of ZnO NMs (RT.pH(x) and RT.pH(x).C)

ZnO was synthesized at RT using the procedure outlined in [57,70]. Initially, 4 g of ZnAc salt was dissolved in 100 mL of deionized water, and NaOH was gradually added to adjust the pH. The resulting solutions underwent bath sonication at RT for 2 h, producing colloidal precipitates that were filtered, washed with water and MeOH several times, and air-dried overnight. For comparison purposes, ZnO was synthesized in solutions with varying pH levels, specifically at pH values of approximately 7 (neutral), 9 (moderate basicity), 11, and 13 (high basicity). While a portion of the synthesized powders was set aside for characterization, the remaining portion underwent calcination at 500 °C for 2 h in an air environment.

The RT.ZnO samples were labeled as RT.pH(x) and RT.pH(x).C according to their preparation conditions, with the "x" symbol denoting the initial pH of the aqueous solution (pH ≈ 7, 9, 11, and 13) and the inclusion of "C" to indicate calcination at 500 °C. For instance, RT-ZnO prepared under neutral pH conditions (pH~7) was designated as RT.pH7, and when subjected to calcination, it was labeled as RT.pH7.C.

2.4. Characterization

Surface morphology was observed by scanning electron microscopy (SEM, Hitachi SU-8230, Minato-ku, Tokyo, Japan). Raman spectra, covering the range of 100–1000 cm^{-1} at RT in the air, were acquired using a Renishaw Raman microscope (inVia) equipped with a 532 nm incident laser. Thermal characteristics were analyzed through thermogravimetric analysis (TGA, TA Instruments, TGA Q500, New Castle, DE, USA) with a heating rate of 10 °C min^{-1} from 30 °C to 1000 °C in the open air. Dynamic light scattering (DLS) analysis at a wavelength of 633 nm was performed using a particle size analyzer (Malvern, Zetasizer Nano S90, Malvern, Worcestershire, UK) featuring a 4 mW laser and an avalanche photodiode detector (APD). The specific surface area of ZnO NMs was determined via the Brunauer–Emmett–Teller (BET) method utilizing a BET surface area analyzer and porosimetry system (TMAXCN, Xiamen Tmax Battery Equipments Limited, Xiamen, China) with nitrogen porosimetry. Fourier transform infrared spectroscopy (FTIR, Thermo Scientific Nicolet 4700, Madison, WI, USA) was employed to investigate ZnO surface functionalization. Absorbance spectra and the optical bandgap of the NMs were obtained using a UV/VIS/NIR spectrophotometer (PerkinElmer, Lambda 750, Waltham, MA, USA).

The bandgap energy (Eg) can be determined from the UV absorption spectrum using the Tauc plot method (Equation (1)) [64].

$$Ah\nu = A(h\nu - E)^n \quad (1)$$

where A is a constant and "n" is the Tauc exponent, which depends on the nature of the electronic transition (commonly n = 1/2 for direct allowed transitions and n = 2 for indirect allowed transitions). The material's Eg can be determined by plotting $(\alpha h\nu)^2$ versus the photon energy ($h\nu$) and extrapolating the linear portion of the plot to the *x*-axis. This method is beneficial for analyzing the optical properties of disordered or amorphous semiconductors.

2.5. Ink Formulation and Preparation of chemiresistive ZnO NMs-Based Sensors

The sensing nanocomposite paste was formulated (Figure 1) from optimized ZnO, Gt, and Ps quantities. The preparation procedure matches our previously developed sensing nanocomposites [71–73]. Initially, 110 mg (~65 wt%) of ZnO NMs and 30 mg (~18 wt%) of Gt flake powder were sonicated for five minutes in 10 mL of xylene solvent using a sonic dismembrator (Fisher Scientific, Hampton, NH, USA) Model 500 with a 0.5 in. diameter tip operating at 30 W to create a well-dispersed mixture (Figure 1A). Subsequently, the nanocomposite mixture was centrifuged to separate it at the bottom of the vial (Figure 1B). After decanting the supernatant, 120 µL (~17 wt%) of a 250 mg mL^{-1} PS solution in xylene was added to form a paste (Figure 1C). The ZnO NMs selected for sensor fabrication at the optimized pH exhibited superior properties as determined through comprehensive characterization. Furthermore, sensors were fabricated using both pre-calcinated and post-calcinated ZnONMs.

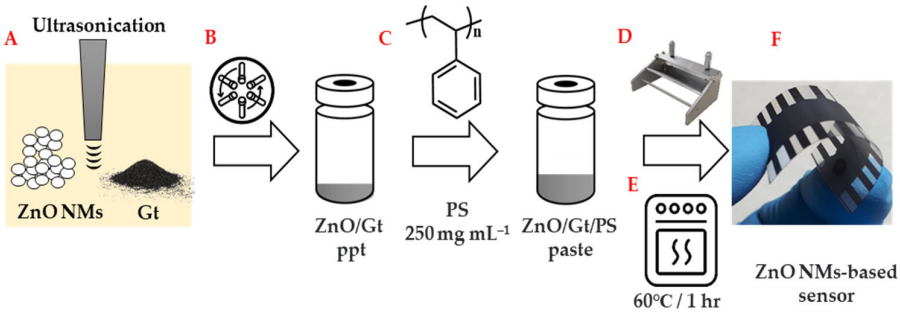

Figure 1. Schematic illustration of the preparation procedure for the ZnO-based gas sensor. (**A**) Sonication of ZnO NMs and Gt flake powder for five minutes in 10 mL of xylene solvent. (**B**) Centrifuge the dispersion to separate the mixture at the bottom of the vial. (**C**) Add PS solution to the mixture to form a paste. (**D**) Spread the paste evenly onto flexible pre-screen-printed carbon electrodes on a PET substrate using the doctor blade method. (**E**) Dry the as-fabricated sensor in an oven at a moderate temperature of 60 °C for 1 h. (**F**) An image of the as-fabricated sensor.

The doctor blade method spread the paste evenly onto flexible pre-screen-printed carbon electrodes on a polyethylene terephthalate (PET) substrate, facilitating sensor fabrication (Figure 1D). Carbon ink (LOCTITE EDAG 423SS E&C, Irvine, CA, USA) from Henkel Co. was used to produce carbon electrodes. Subsequently, the sensors were dried for one hour in an oven at a moderate temperature of 60 °C (Figure 1E). The screen-printed carbon electrodes featured a 1 mm space between two adjacent electrodes, measuring 15 mm in length, 20 mm in width, and 5 µm in thickness. The resulting sensing thin films were 10 mm long, 20 mm wide, and 6 µm thick (Figure 1F). Under standard air conditions, the as-fabricated sensors exhibited a resistance range of 100–200 kΩ.

2.6. Evaluation of the Sensing Performance of the ZnO NMs-Based Sensors

The chemiresistive gas sensing performance (sensors' sensitivity and selectivity) was evaluated using the Nextron microprobe station (Figure S1, Peltier-type sample stage, Seoul, Republic of Korea) [74]. Please refer to the Supporting Information for a comprehensive overview of the station's specifications and features. The electrical resistance in the sensing thin films, positioned between two precisely adjacent carbon electrodes, was systematically monitored over time in response to diverse gases, including acetone (C_3H_6O), NH_3, triethylamine (($C_2H_5)_3N$), acetic acid ($C_2H_4O_2$), alcohols (methanol (MeOH, CH_3OH), ethanol (EtOH, C_2H_5OH), isopropanol (IPA, C_3H_7OH)), aldehydes (dimethyl-6-octenal ($C_{10}H_{18}O$), hexanal ($C_6H_{12}O$), acrolein (C_3H_4O), butyraldehyde (C_4H_8O), formaldehyde (CH_2O), pentanal ($C_5H_{10}O$), acetaldehyde (CH_3CHO)), and aromatics (benzene (C_6H_6) styrene (C_8H_8)). We used a lab-made organic solvent gas generator that unfolds between liquid and vapor. Please refer to the Supporting Information for an overview of the gas generator working principle.

A programmed multimeter connected to a PC via an Arduino card collected the sensors' electrical resistance. Equation (2) defines the sensor response to gas, humidity, and temperature variations. When assessing the sensors' response to gas, R_1 measures their electrical resistance under the initial conditions (RT and RH ≈ 30–40%), and R_2 reflects the resistance following exposure to gas at the same environmental parameters (RT and RH ≈ 30–40%). After achieving a steady state with the gas exposure, sensors were left to recover by exposing them to the initial state (i.e., RT and RH ≈ 30–40%) upon opening the chamber's lid. Response and recovery times correspond to the duration required to reach 90% of the total resistance change after exposure to gas and air.

Additionally, the sensors' performance temperature and RH variation were investigated. The sensors' response to temperature was conducted from −20 °C to 170 °C at RH ≈ 10%, and the sensors' performance against humidity was investigated across RH levels from 10% to 90% at 20 °C. When evaluating the sensors' response to temperature changes, R_1 captures their resistance in the initial state (20 °C and RH~10%), and R_2 denotes the resistance subsequent to adjusting the temperature, without exposure to gas and maintaining the initial RH~10%. Similarly, when analyzing the sensors' response to RH, R_1 represents theirresistance in the initial state (20 °C and RH~10%), while R_2 indicates the resistance after adjusting the RH, without gas exposure and maintaining the initial temperature conditions (20 °C).

$$\text{Response}(\%) = \left(\frac{R_2 - R_1}{R_1}\right) \times 100 \quad (2)$$

2.7. Evaluation of the Mechanical Flexibility of the ZnO NMs-Based Sensor

The sensors' mechanical flexibility was evaluated by assessing their ability to withstand stress and strain through repetitive bending at a predetermined critical angle. The critical angle was determined by subjecting the sensors to gradual bending in 5° increments while monitoring the change in electrical resistance, which was calculated using Equation (2) with R_2 corresponding to the bent sensor resistance. Subsequently, repetitive bending cycles were performed at a bending rate of 5° per second (5° s^{-1}) up to their critical angles. We maintained a bias voltage of 6 V throughout these assessments, using a Keithley sourcemeter (Keithley 2601A sourcemeter). The results are presented as changes in electrical resistance, as calculated by Equation (2). These experiments were conducted under ambient conditions.

3. Results and Discussion

The formation of ZnO in a basic aqueous solution at RT using $Zn(CH_3COO)_2$ salt and NaOH involves dissociation, complexation, and dehydration reactions [63,75]. $Zn(CH_3COO)_2$ salt is the source of zinc ions (Zn^{2+}), and NaOH is the base. The mechanism generally proceeds by dissociation of $Zn(CH_3COO)_2$ salt when added to water, giving Zn^{2+} and acetate ions

(CH_3COO^-) (Equation (3)) [75]. Next, Zn^{2+} reacts with hydroxide ions (OH^-), forming a soluble zinc hydroxide complex ($[Zn(OH)_4]^{2-}$, Equation (4)) [63]. When the concentration of the complex ions becomes sufficiently high, ($[Zn(OH)_4]^{2-}$ can start forming cloudy colloidal particles to precipitate at the bottom of the reactor ($Zn(OH)_2$, Equation (4)) [63]. Finally, the $Zn(OH)_2$ formed in the previous step can then be converted to ZnO through heating, such as in a hydrothermal reaction, or by aging the solution at RT (Equation (5)) [63,75]. The specific process can be influenced by temperature, time, and reactant concentration [14].

$$Zn(CH_3COO)_2(aq) \rightarrow Zn^{2+}(aq) + 2CH_3COO^-(aq) \quad (3)$$

$$Zn^{2+}(aq) + 2OH^-(aq) \rightarrow [Zn(OH)_4]^{2-}(aq) \rightarrow Zn(OH)_2(s) \quad (4)$$

$$Zn(OH)_2(s) \rightarrow ZnO(s) + H_2O \quad (5)$$

The fate of CH_3COO^- ions during the ZnO formation can be influenced by factors such as pH, temperature, and the presence of other species [75]. Furthermore, it depends on their solubility and the overall conditions of the reaction. If the conditions favor the solubility of CH_3COO^- ions, they may persist in the solution throughout the process. Alternatively, if conditions promote the formation of insoluble CH_3COO^- salts, these salts may precipitate along with or separate from the $Zn(OH)_2$ precipitation.

CH_3COO^- ions originate from the dissociation of acetic acid (CH_3COOH) in water [76]. The pH of the solution influences the equilibrium between CH_3COOH and CH_3COO^- ions. In a basic solution, as the pH increases, the equilibrium shifts towards the deprotonation of CH_3COOH, leading to an increased concentration of CH_3COO^- ions [77]. They are less likely to undergo further reactions or hydrolysis and can persist in the solution without significant changes. Still, CH_3COO^- ions can participate in complex formation reactions, especially with metal cations. Therefore, the solution basicity can impact the behavior of CH_3COO^- ions by influencing their ionization, stability, complex formation, and contribution to precipitation reactions [77]. Understanding these effects is essential for controlling the synthesis process and tailoring the properties of the final ZnO product.

Compared with the hydrothermal method, the ZnO formation typically involves the reaction of a zinc source, often $Zn(NO_3)_2$, with a hydrolyzing agent, such as $C_6H_{12}N_4$ [78]. Briefly, $Zn(NO_3)_2$ dissolves readily in water to form a clear aqueous solution. $C_6H_{12}N_4$ serves as a hydrolyzing and complexing agent upon addition to the $Zn(NO_3)_2$ solution. When the precursor solution is sealed in a high-pressure reactor and heated to a specific temperature, typically 80 °C to 200 °C [79], HMTA reacts with water to release the NH_3, CH_2O, and OH^- groups (Equation (6)) [78]. As the hydrothermal reaction proceeds, the Zn^{+2} ions from the $Zn(NO_3)_2$ react with the OH^- groups (Equation (4)) generated from the HMTA hydrolysis. The formed $Zn(OH)_2$ eventually decomposes into ZnO and water (Equation (5)). ZnO NPs or crystallites grow and precipitate in the reaction vessel as the reaction progresses. The hydrothermal method is a versatile approach for the controlled synthesis of ZnO and other NMs [78].

$$C_6H_{12}N_4 + 6H_2O \rightarrow 6NH_3 + 6CH_2O + 6OH^- \quad (6)$$

The hydrothermal conditions, characterized by a high temperature and pressure, can expedite the conversion of $Zn(OH)_2$ into ZnO more rapidly, potentially yielding smaller and more crystalline ZnO particles [80]. In contrast, the reaction at RT proceeds more slowly and may result in larger and less crystalline particles [81]. Thus, precise control of reaction conditions, including temperature, pressure, and reaction time, is crucial to achieve the desired characteristics of the ZnO NMs. The specific reaction conditions and parameters can be tailored based on the desired outcomes, allowing modifications to control the size, shape, and properties of the ZnO NMs.

This study compares the characteristics of ZnO NMs prepared at RT with those synthesized through the typical hydrothermal process (hyd.C). The hyd.C was prepared at 90 °C for 6 h, followed by calcination at 500 °C for two hours in the air. In contrast, the

RT.pH(x) NMs were synthesized at RT using bath sonication for 2 h. Furthermore, the properties of RT.pH(x) NMs were systematically evaluated by varying the initial aqueous solution's basicity, ranging from neutral pH~7 to a high basicity at pH~13. The influence of the calcination process at 500 °C for 2 h in the air was also examined.

An arsenal of characterization techniques was deployed to understand the synthesized ZnO NMs' properties comprehensively. FTIR was conducted to assess the chemical composition of the NMs and to explore potential interactions among their components. Figure 2 presents the FTIR spectra for hyd.C, RT.pH(x), and RT.pH(x).C. The FTIR spectrum for hyd.C exhibited a broad peak ranging between 3000 cm^{-1} and 3700 cm^{-1} for the O-H and C-H stretching peaks [43,82,83], and well-defined peaks at approximately 1640 cm^{-1} and 1500 cm^{-1} which are commonly attributed to the C=O stretching vibrations [69,84], and 1365 cm^{-1} whichcan be attributed to the symmetrical C-O vibrations bond [43,83]. Peaks that appeared in the spectra between 800 and 500 cm^{-1} are associated with the Zn-O stretching vibration mode [10,43].

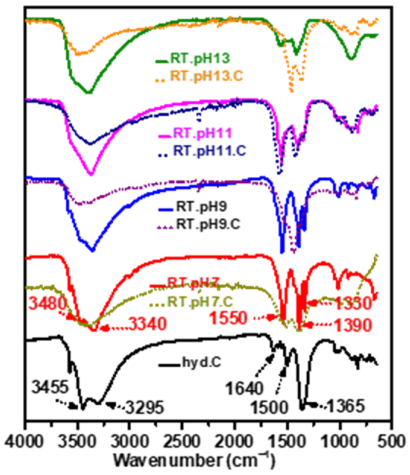

Figure 2. FTIR spectra analysis of hyd.C, RT.pH(x), and RT.pH(x).C.

The FTIR analysis of RT.pH(x) (prior to calcination) indicated a minimal alteration in the peaks associated with the O-H/C-H functional groups (3000 cm^{-1} to 3700 cm^{-1}). In contrast, RT.pH(x) exhibited distinct changes, manifesting stretching peaks at 1550 cm^{-1} attributed to C=O stretching vibration [69], 1390 cm^{-1}, and 1330 cm^{-1} linked to the bending vibration of the C-O bond [82,85]. In the FTIR analysis of RT.pH(x).C (post calcination), the peak related to the O-H functional groups noticeably diminished, suggesting a reduction or removal of these groups at high temperatures during the calcination process.

Notably, in the case of RT.pH7.C, the intensity of the O-H functional group peaks was highest, indicating a partial reduction at 500 °C. As the pH increased to 13, these peaks diminished, signifying a reduction in the concentration of O-H functional groups. The observed spectral changes highlight a transformation in the material's chemical composition due to the elevated temperature treatment, emphasizing the significant impact of solution pH and thermal processes on the formation and concentration of these functional groups in the synthesized material.

The TGA analysis unveiled distinct variations among the ZnO NMs, providing crucial insights into their thermal behavior. Notably, in the case of hyd.C, a consistent absence of decomposition patterns was observed throughout the temperature range of 20 °C to 1000 °C, as shown in Figure 3B. This aligns with the typical thermogram expected for ZnO NPs and signifies the absence of burnable organic materials within the hyd.C sample.

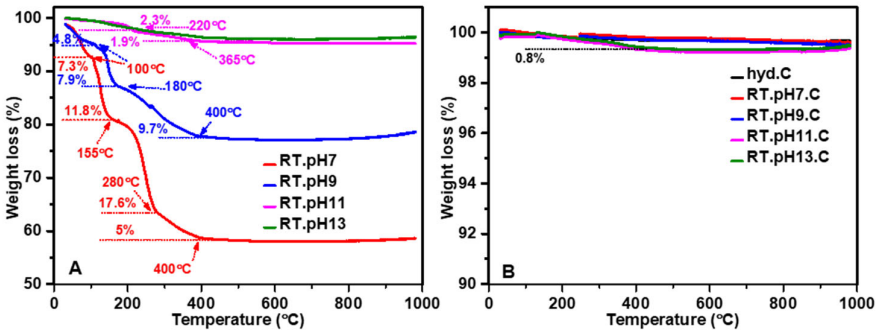

Figure 3. TGA thermogram analysis for (**A**) RT.pH(x), and (**B**) hyd.C and RT.pH(x).C.

A complex multistep decomposition pattern emerged after investigating RT.pH(x) NMs prepared under low pH conditions (pH ≈ 7 and ≈ 9), as shown in Figure 3A. Initially, both RT.pH7 and RT.pH9 displayed a weight loss of 7.3wt% and 4.8wt%, respectively, between 30 °C and 100 °C, primarily attributed to evaporating adsorbed water molecules. Subsequently, a second decomposition step occurred at 155 °C and 180 °C, resulting in an additional weight loss of 11.8 wt% and 7.9 wt% for RT.pH7 and RT.pH9, respectively. Further analysis revealed that RT.pH7 demonstrated a two-step decomposition pattern, accounting for a 17.6% and 5% weight loss between 155 and 280 °C and 280 and 400 °C, respectively. In contrast, RT.pH9 exhibited one additional decomposition step of 9.7% between 180 and 400 °C. After these decomposition patterns, the total weight loss for RT.pH7 and RT.pH9 amounted to 41.7% and 22.4%, respectively. This observation suggests the presence of substantial organic impurities persisting with ZnO NMs using low pH conditions (pH~7 and pH~9). Nevertheless, an organic complex involving CH_3COO^- ions appeared at pH~7, which heightened the presence of organic material. This aligns with the observation of the continued presence of a broad peak attributed to O-H groups in FTIR after calcination.

In contrast, during TGA analysis, ZnO materials prepared at higher pH levels (pH 11 and 13) exhibited only a marginal weight loss of 4.2% (2.3% + 1.9%) up to 365 °C and maintained their thermal behavior for the rest of the experiment [86]. This observation strongly suggests the absence of combustible organic materials within these samples. The phenomenon can be attributed to equilibrium shifts favoring the deprotonation of CH_3COOH, resulting in an increased concentration of CH_3COO^- ions that could be effectively removed during the filtration step. Therefore, lower organic impurities can be found with the synthesized ZnO NMs.

Subsequent to calcination, all RT.pH(x).C samples displayed a minimal weight loss, reaching a maximum of 0.8% between RT and 400 °C [83]. This signifies the successful removal of organic materials through the calcination process. These TGA results offer crucial insights into the presence or absence of organic materials within the ZnO NPs and underscore the impact of diverse preparation conditions and post-treatment processes on the material's composition and purity.

In a typical XRD diffractogram of ZnO, distinctive peaks are observed at 2θ values of 32, 35, 37, 47, 57, 63, 67, 68, 69, 73, and 77, which can be attributed to specific crystallographic planes of (100), (002), (101), (102), (110), (103), (200), (112), (201), and (101), respectively [57]. The XRD diffractogram of hyd.C closely resembled the typical ZnO diffractogram, as seen in Figure 4A. However, the XRD patterns for the RT.pH(x) series once again indicated a clear dependence on the initial solution's basicity during the ZnO formation process (Figure 4A). In the case of RT.pH7, a very different diffractogram was observed. This difference can be attributed to the high percentages of remaining organic materials, which constituted up to 41.7% of the ZnO powder, as found by the TGA analysis. Matching each peak to a specific material proved challenging, necessitating further research. At a higher basicity (RT.pH9), the XRD pattern closely matched the typical ZnO NP diffractogram. However, a small number of small peaks still appeared, corresponding to the remaining 22.4 wt% of

organic material within the ZnO powder. With even higher basicity solutions (pH ≈ 11 and pH ≈ 13), the XRD patterns produced clear diffractograms that agreed with the typical ZnO NP diffractogram.

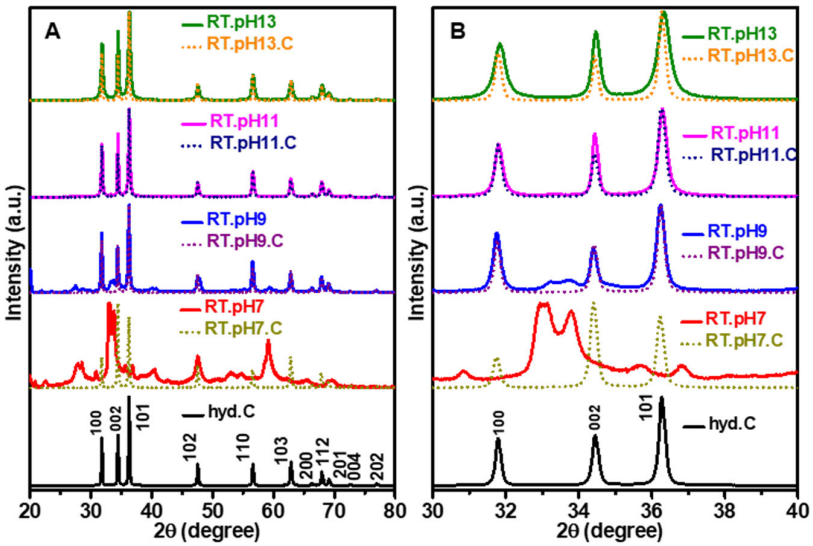

Figure 4. XRD diffractogram analysis of (**A**) hyd.C, RT.pH(x), and RT.pH(x).C, and (**B**) magnification for 2θ between 30° and 40°.

Following the calcination process, all samples within the RT.pH(x).C series displayed clear XRD diffractograms (Figure 4A) that matched the typical ZnO NP diffractogram, confirming the removal of organic materials, as observed in the TGA analysis. Notably, the variation in the XRD intensity peaks at 2θ ≈ 32, 35, and 37 for RT.pH(x).C compared to the ones before calcination (i.e.,RT.pH(x)) can be attributed to possible structural transformation, particularly for the ZnO NMs prepared at pH 11 and 13 (Figure 4B). These XRD findings provide insights into the crystalline structure of ZnO NPs and how they are affected by preparation conditions and post-treatment processes.

The morphology of the ZnO NMs was searched through SEM, as seen in Figure 5. The SEM images of (hyd.C) depicted NPs forming between 75 nm and 200 nm (Figure 5A). In contrast, the particle shape and size of RT.pH(x) exposed a distinctive pattern and were found to be intricately linked to the solution's basicity levels. At pH 7 (RT.pH7), the particles exhibited a compact sheet-like structure (Figure 5B). Moving to pH 9 (RT.pH9), the ZnO NMs transformed into a mixture of large semi-hollow tubes exceeding 200 nm alongside flakes and NPs (Figure 5D). It appears that the large flakes formed at pH~7 were influenced by the solution's basicity (pH~9), leading to their wrapping and the formation of semi-hollow tubes. At pH 11 (RT.pH11), the ZnO material comprised exfoliated nanosheets with dimensions falling within 500 nm to 900 nm, maintaining a thickness ranging between 2 nm and 6 nm (Figure 5F). Nevertheless, large and small particles with diameters of approximately 350 nm were formed. At the highest basicity level of pH 13 (RT.pH13), the ZnO NMs adopted a more traditional spherical shape, ranging in size from 20 nm to 40 nm (Figure 5H). These NPs aggregated into larger structures, reaching sizes between 100 nm and 200 nm.

A notable morphological transformation occurred following calcination. The initial RT.pH7.C compact, sheet-like structure transitioned into NPs with sizes ranging between 35 nm and 180 nm (Figure 5C). Similarly, RT.pH9.C exhibited the formation of NPs while retaining the presence of large tubes (Figure 5E). RT.pH11.C showcased a structural shift from exfoliated nanosheets to NPs, gathering in substantial clusters with sizes ranging from 140 nm to 380 nm (Figure 5G). At the highest basicity level (RT.pH13.C), the NPs that initially formed at RT underwent nucleation, aggregating into clusters with sizes between 190 nm and 280 nm (Figure 5I).

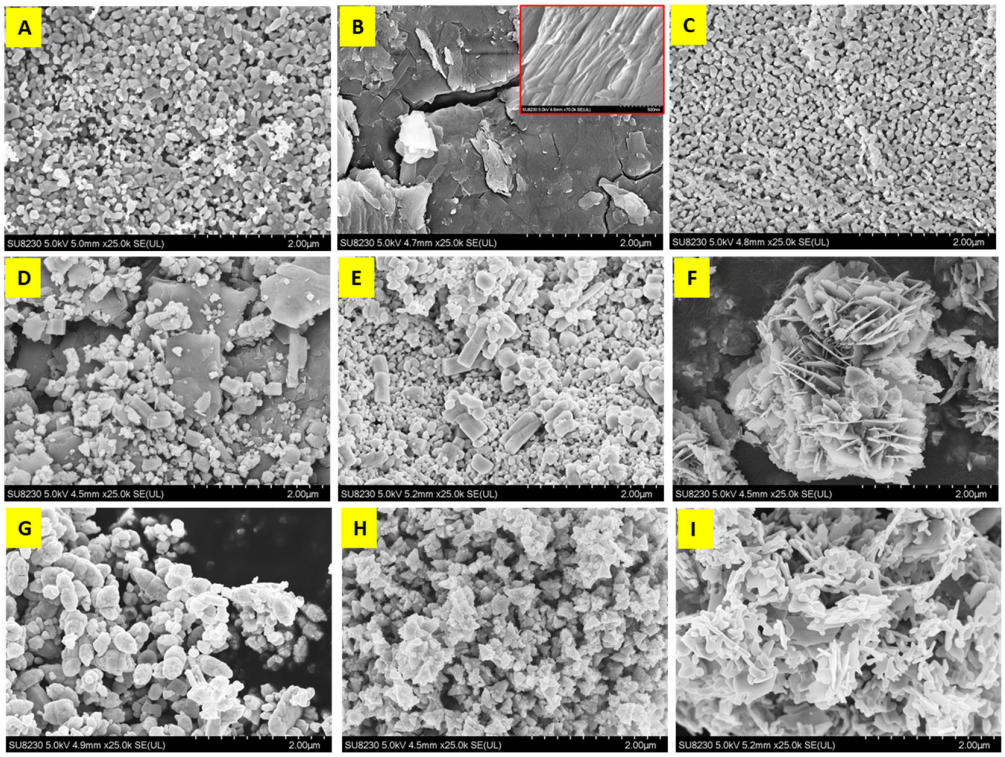

Figure 5. SEM analysis of (**A**) hyd.C, (**B**) RT.pH7, (**C**) RT.pH7.C, (**D**) RT.pH9, (**E**) RT.pH9.C, (**F**) RT.pH11, (**G**) RT.pH11.C, (**H**) RT.pH13, and (**I**) RT.pH13.C.

This structural transformation coincided with a decrease in the concentration of O-H functional groups and the elimination of remaining organic materials through calcination, as observed in the FTIR and TGA analyses. These findings underscore the significant impact of pH levels and the calcination process on the morphology and size of ZnO NPs, providing insights into their responsiveness to varying chemical conditions.

DLS served as a comprehensive tool for assessing the mean NP size distribution of the prepared materials, considering both solution basicity and the calcination process. As illustrated in Figure 6A, hyd.C exhibited a broad NP distribution spanning from 500 nm to ~1.5 µm. In contrast, RT.pH(x) materials also displayed a wide NP distribution in lower size ranges. At alow solution basicity (pH~7 and pH~9), NP distribution for RT.pH7 and RT.pH9 fell within 170–850 nm and 250 nm–1.1 µm, respectively. Higher basicity solutions resulted in narrower NP size distributions following the basicity increase. RT.pH11 displayed a distribution over the 120 nm–1 µm range, while RT.pH13 exhibited a narrower distribution ranging from 360 to 750 nm.

Following calcination, RT.pH(x).C demonstrated notable NP distribution changes, aligning with SEM observations. RT.pH7.C showcased a reduction in NP distribution to 315–850 nm. RT.pH9.C exhibited two NP distributions: the first spanning from 160 to 440 nm and the second covering a broader range of 440 nm–2 µm. This aligned with the SEM observation of the formation of the NPs and nanotubes mixture. Regarding high basicity, RT.pH11.C separated into two narrow NP distributions within the pre-calcination range, spanning 215–375 nm and 375–735 nm. Similarly, RT.pH13.C displayed two ranges, with the majority of NPs sized between 100 nm and 360 nm, while a smaller percentage maintained sizes within the pre-calcination range of 360 nm to 750 nm. The SEM and DLS analysis demonstrate the formation of NPs using a high-basicity solution at RT, indicating the potential to bypass the costly and time-consuming calcination process typically associated with hydrothermal synthesis. It eliminates the need for complex tools, lengthy synthesis steps, and harsh conditions such as high synthesis and calcination temperatures.

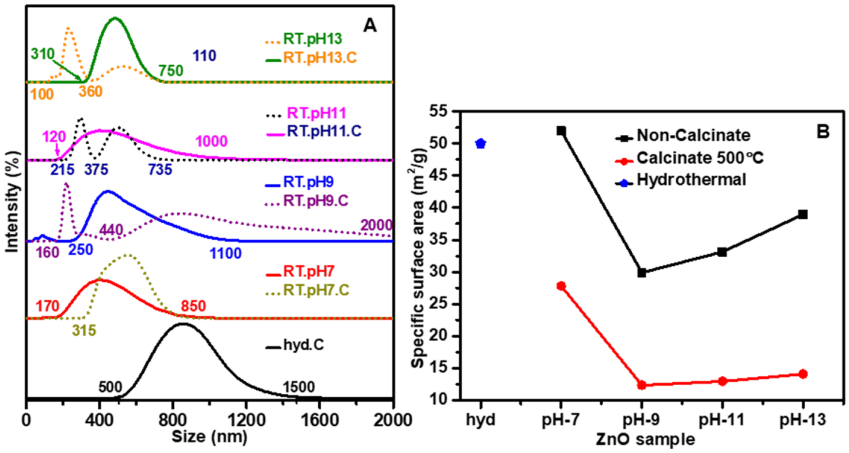

Figure 6. (**A**) DLS Analysis of NP size distribution of hyd.C, RT.pH(x), and RT.pH(x).C. (**B**) BET analysis for hyd.C, RT.pH(x), and RT.pH(x).C.

As measured by the BET technique, ZnO NPs' specific surface area fell in the 4–126 m^2 g^{-1} range [87–89]. Figure 6B summarizes the specific surface area values for hyd.C, RT.pH(x), and RT.pH(x).C. Whereas Hyd.C produced NPs with a specific 50 m^2 g^{-1} surface area, the RT.pH(x) series exhibited notable differences in the specific surface areas before and after calcination at 500 °C for 2 h. Among the RT.pH(x) samples, RT.pH7 displayed the highest specific surface area, measuring approximately ~52 m^2 g^{-1}. This increase can be attributed to a relatively high concentration of organic material (45 wt%) within the ZnO NPs. As the solution's basicity levels increased through the ZnO NPs synthesis, the specific surface area decreased, measuring approximately 30 m^2 g^{-1} for RT.pH9, followed by a gradual increase to 33.1 m^2 g^{-1} for RT.pH11 and 39 m^2 g^{-1} for RT.pH13. A substantial reduction in the specific surface area was observed after the calcination process. Specifically, RT.pH7.C underwent a reduction to 27.8 m^2 g^{-1}, equivalent to a 46.5% decrease. This reduction can be attributed to the removal of organic materials during the calcination process and the structural transformation, as noticed by SEM analysis. The remaining samples within the RT.pH(x).C series showed a closely matched specific surface area, falling within the 12 to 14 m^2 g^{-1} range, indicating a reduction in the specific area between 60% and 64%. The close match between the specific surface areas can be attributed to the close match in structural transformation after calcination, mainly caused by the formation of NPs.

The characteristic UV–Vis absorbance peak of ZnO NPs highlighted discernible differences within the 340 nm to 380 nm range, contingent upon their respective preparation conditions, as seen in Figure 7A. In contrast, hyd.C induced an absorbance peak at 375 nm, attributed to the transition occurring within the oxygen functional groups [90], and indicating NP formation [91,92]. Notably, the UV–Vis absorption spectra of RT.pH(x) and RT.pH(x).C exhibited a close resemblance, irrespective of the calcination process, and showcased an absorbance profile similar to hyd-C.

However, both RT.pH(x) and RT.pH(x).C revealed a slight blue shift in the absorbance peak towards lower wavelengths, from 375 nm to 360 nm. This shift, accompanied by an elevation in basicity during the initial preparation conditions, suggests alterations in the electronic structure or environment of the material. This implies that the material absorbs light at shorter wavelengths, corresponding to higher energy. Despite this, bandgap measurements for hyd.C, RT.pH(x), and RT.pH(x).C (Figure 7B) exhibited a consistent 3.0 eV bandgap, aligning with the existing literature [93].

Therefore, the blue shift in the absorbance peak may not solely be attributed to changes in bandgap but may also signify the formation of smaller-sized NPs compared to those found in hyd.C, as supported by SEM and DLS analysis. Other contributing factors to this blue shift include particle size reduction, quantum confinement, surface states, structure defects, and potential doping [92]. Another plausible explanation for the blue shift in the absorbance band is linked to the reduction of oxygen functional groups and elimination

ofimpurities, including organic materials, due to the calcination process, as observed through FTIR and TGA analyses.

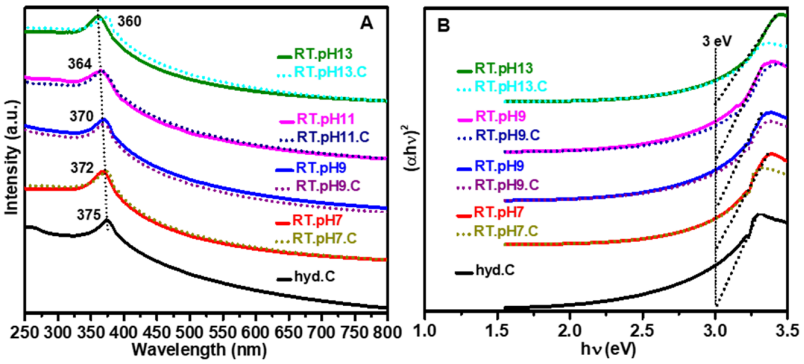

Figure 7. (**A**) UV–Vis absorbance spectra and (**B**) bandgap measurements for hyd.C, RT.pH(x), and RT.pH(x).C.

Raman spectra, spanning from 100 cm^{-1} to 1000 cm^{-1}, were acquired using a Raman microscope (Renishaw, in Via Reflex., Wotton-under-Edge, Gloucestershire, UK) at ambient conditions, employing a 532 nm excitation laser to assess the quality of ZnO NMs, as seen in Figure 8. Commonly observed in the Raman spectra of ZnO NPs are characteristic peaks at 437 cm^{-1}, 381 cm^{-1}, 332 cm^{-1}, and 583 cm^{-1}, corresponding to the vibrational motion within the crystal lattice (E_2(high), A_1(TO), $2E_2$(M), and E(LO), respectively) [83].

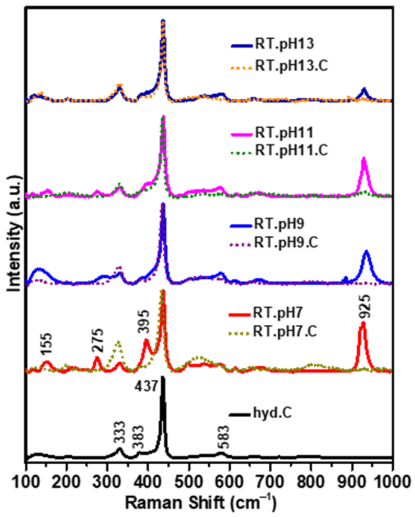

Figure 8. Raman analysis of NP size distribution of hyd.C, RT.pH(x), and RT.pH(x).C.

In the Raman analysis of hyd.C, a close match to the typical ZnO NP Raman spectrum was observed, indicating the formation of NPs as observed by SEM analysis. In contrast, the RT.pH(x) displayed a typical Raman spectrum. However, distinctive Raman peaks emerged at 155 cm^{-1}, 275 cm^{-1}, and 925 cm^{-1}, attributed to residual CH_3COO^- impurities within the formed ZnO NPs. Notably, the intensity of these peaks diminished with an increase in solution basicity, reaching its lowest point at pH~13. This reduction is attributed to an equilibrium shift toward the deprotonation of CH_3COOH at a high basicity, favoring the formation of CH_3COO^- ions. These ions can be effectively eliminated through filtration, enhancing the ZnO NPs' purity. The RT.pH(x).C samples revealed the elimination of peaks associated with organic impurities through calcination. This resulted in the production of the typical ZnO Raman spectra, indicating successful purification of the ZnO NPs.

The initial characterization underscored the efficiency of forming ZnO NPs at RT, particularly at pH~13, revealing minimal carbon impurities and the production of well-

crystallized, small-sized NPs. This streamlined process eliminates the necessity for expensive and time-consuming calcination procedures. The encouraging outcome propels us to delve into applying these formed NPs in developing flexible gas sensors. Our subsequent steps involve a comprehensive investigation into the efficiency and effectiveness of these materials for gas sensing applications.

Two chemiresistive flexible gas sensors were fabricated, containing pre- and post-calcinated ZnO NPs prepared with a pH level of pH~13 (i.e., RT.pH13 and RT.pH13.C). The fabrication process involved the deposition of ZnO-based nanocomposite pastes onto a pre-printed carbon electrode over a PET substrate using the doctor blade technique. These nanocomposite pastes, formulated in xylene solvent, were composed of a blend wherein RT.pH13 and RT.pH13.C ZnO NPs served as the core sensing material. Gt flakes were incorporated as the conductive material to enhance thin film conductivity while adding PS to ensure the thin film's structural integrity and mechanical flexibility. Following the deposition process, the sensors underwent an air-drying period for 1 h at 60 °C, facilitating the evaporation of the xylene solvent.

The sensitivity of the sensors was systematically evaluated by exposing them to various gases with different polarities as indicated by dipole moments (D) at a concentration of 200 ppm, revealing distinct sensitivity profiles based on calcination. The (RT.pH13)-based sensor exhibited superior sensitivity towards C_8H_8 (styrene, 0.1 D) and $C_2H_4O_2$ (acetic acid, 1.74 D) with responses of 590 and 140, respectively, as depicted in Figure 9A,B. In addition, the (RT.pH13)-based sensor exhibited lower sensitivity to $C_{10}H_{18}O$ (dimethyl-6-octenal, 2.5–3.5 D) with a response of 29. In contrast, the (RT.pH13.C)-based sensor maintained its sensitivity to C_8H_8 and $C_2H_4O_2$, but lower responses of 450 and 75, respectively, were observed. Additionally, the (RT.pH13.C)-based sensor showed a lower response to $C_{10}H_{18}O$ of 12, but heightened sensitivity toC_6H_6 (benzene, 0 D), C_3H_6O (acetone, 0.355 D) and C_2H_5OH (EtOH, 1.66 D) gases with responses of 49, 19, and 26, respectively, surpassing the responses of 2, 4, and 11 recorded by the (RT.pH13)-based sensor. While a definitive correlation between the sensors' sensitivity and their response to gases' dipole moments remains elusive, it is noteworthy that the sensing performance exhibited variations corresponding to the structural transformations of the NMs following the calcination process. Noteworthily, ZnO NP-based sensors in the literature have exhibited notable affinity towards gases such as H_2S and NO_2 [19,94,95], which were not available during the sensors' initial sensing performance investigation. Consequently, further testing with a broader array of gases is imperative to ensure a comprehensive evaluation and validation of the sensors' capabilities.

The gas sensing mechanism involves interactions between gas molecules and active sites on the ZnO surface. Knowing that the RT.pH13 and RT.pH13.C closely matched in crystallinity, physical structure, and bandgap, the observed differences in surface area, particle size, and the presence of impurities between RT.pH13 and RT.pH13.C NPs are significant factors influencing gas sensing properties. RT.pH13 NPs exhibited a larger particle size range (310–750 nm), higher surface area (38.96 m^2g^{-1}), and relatively higher organic residual impurities. In contrast, RT.pH13.C NPs had a reduced particle size, falling within ranges of 100–360 nm and 100–750 nm, a reduced surface area (14.08 m^2g^{-1}), and fewer organic residual impurities, suggesting a cleaner surface. These alterations in surface properties may lead to changes in the sensor's affinity for specific gas molecules. Nevertheless, further research is necessary to gain a deeper understanding of the impact of calcination on the sensor's interaction with various gas molecules.

Figure 9C illustrates the sensor responses to a gradual increase in C_8H_8 gas concentrations from 10 ppm to 100 ppm. Notably, the (RT.pH13)-based sensor exhibited a progressive response escalation with the styrene gas concentration, rising from 6.7% at 10 ppm to 142% at a 100 ppm C_8H_8 concentration, as depicted in Figure 9C (inset). In contrast, the (RT.pH13.C)-based sensor demonstrated a lower response of 2.6% at 10 ppm, a slight increase to 6.7% at 80 ppm C_8H_8 gas concentration, spiking to 31% at 100 ppm C_8H_8 concentrations. The (RT.pH13)-based sensor displayed partial recovery after evacuating the gas chamber, while the (RT.pH13.C)-based sensor fully recovered the initial

response signal at low C_8H_8 concentrations. While (RT.pH13)- and (RT.pH13.C)-based sensors were evaluated at RT, the latest styrene sensors that can be potentially used for lung disease diagnosis required elevated temperatures within the range of 120–260 °C [96–98]. These high temperatures pose challenges for certain industrial applications and impede the development of flexible sensors on low-cost substrates. On the contrary, the recently developed RT operating styrene sensors exhibited inferior response, recording a response below 100, when exposed to 100 ppm C_8H_8 gas concentration as observed in the cases of Ni-MoS_2-based sensors [99].

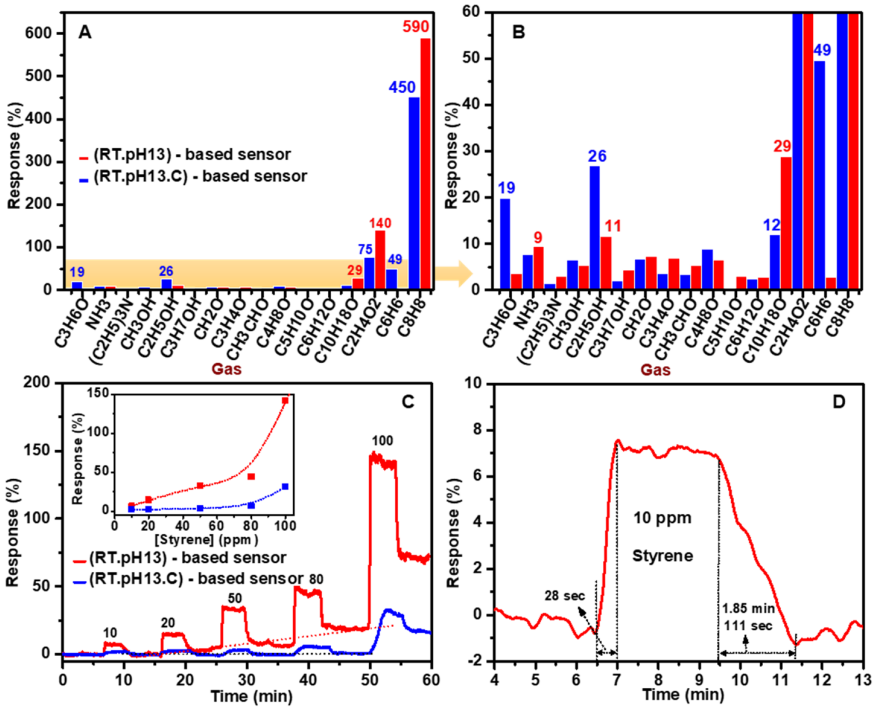

Figure 9. The response (electrical resistance change %) of (RT.pH13)-based sensor and (RT.pH13.C)-based sensor at RT and RH of 30–40% is depicted in (**A**) a series of gases at concentrations of 200 ppm. The magnified view in (**B**) illustrates the sensors' response to the gases. (**C**) The sensors' response to wise C_8H_8 gas concentration increases between 10 ppm and 100 ppm, while (**D**) highlights the response to a 10 ppm C_8H_8 gas concentration, providing insights into the response and recovery times.

The partial recovery of the (RT.pH13)-based sensor suggests a chemical reaction between styrene molecules and the sensing thin film, leading to a chemical alteration that hinders full response signal recovery. In contrast, the (RT.pH13.C)-based sensor preferred physical sorption of C_8H_8 molecules on the sensor's thin film surface with negligible chemical changes. However, the (RT.pH13.C)-based sensor showed a partial recovery of the response signal at exposure to high C_8H_8 concentrations of 100 ppm, indicating the occurrence of a chemical reaction on the sensor's thin film surface. The likely chemical reaction involves the suspension polymerization of C_8H_8 molecules at low temperatures, such as 60–90 °C and pH 10, where ZnO serves as a suspension agent in producing PS [100]. This formation of non-conductive PS in the sensing thin film could hinder charge transfer, increasing the sensor's electrical resistance (increasing in response).

Figure 9D displays the response and recovery times of the (RT.pH13)-based sensor at a 10 ppm C_8H_8 concentration. The (RT.pH13)-based sensor exhibited a rapid response of 28 s but prolonged recovery of 111 s (1.85 min), indicating a good performance in C_8H_8 detection. Evaluating recovery time at higher styrene exposures (i.e., >10 ppm) posed a considerable challenge due to the sensor's observed partial recovery response, as depicted in Figure S2. This partial recovery phenomenon introduced complexities in accurately determining the recovery time, thus necessitating careful consideration and interpretation

of the data. Ongoing research aims to improve the sensor's performance further and enhance the understanding of its capabilities for real-life applications.

The sensor responses to humidity and temperature were investigated using the Nextron probe station. As that part of the PS material can be lost during the process, initially, the sensors underwent calcination at 180 °C for 10 min to eliminate the low molecular weight of the PS material from the sensor thin film (Figure S3). Subsequently, the sensor responses were assessed to reflect the characteristics of the ZnO/Gt/PS nanocomposite thin film.

In Figure 10A, the (RT.pH13)-based sensor exhibited a distinct behavior. Its electrical resistance increased as the temperature decreased from 20 °C to −20 °C. It then promptly recovered its initial electrical resistance as the temperature returned to 20 °C. Next, only minor changes in electrical resistance between 20 °C and 110 °C were displayed. However, as the temperature increased from 110 °C to 180 °C, the resistance increased, and it consistently recovered its initial resistance as the temperature decreased to 110 °C again. The (RT.pH13)-based sensor showed a similar response behavior to temperature as the temperature decreased from 110 °C to −20 °C.

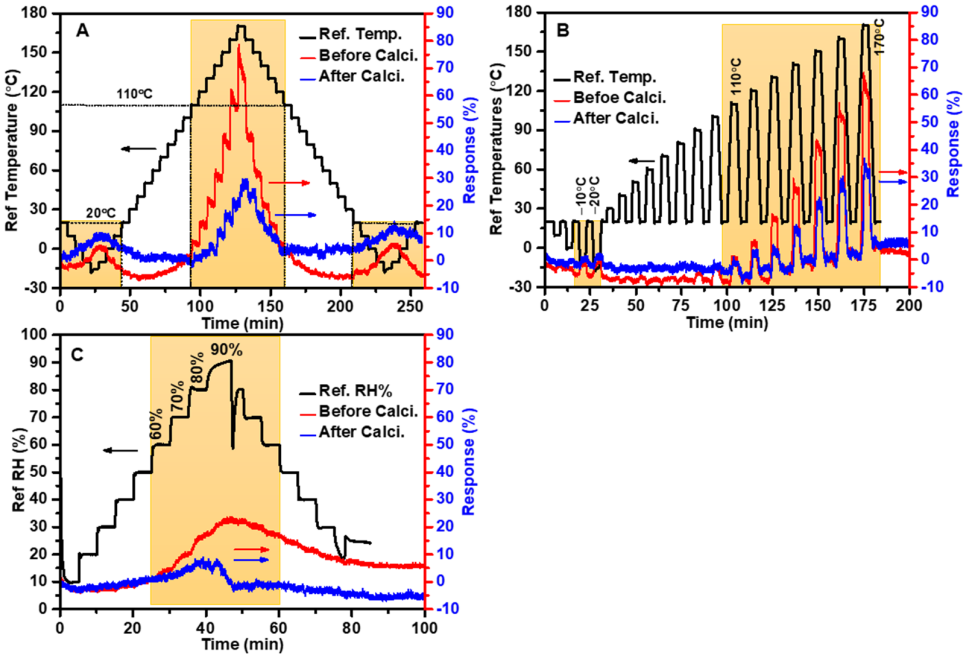

Figure 10. The response (electrical resistance change %) of (RT. pH13) and (RT. pH13.C)-based sensors to (**A**) step-wise temperature changes between −20 °C and 170 °C, (**B**) dynamic response test between −20 °C and 170 °C, and (**C**) varying humidity levels between RH ≈ 10% and 90%.

In contrast, the (RT.pH13.C)-based sensor demonstrated a more consistent behavior, characterized by lower electrical resistance changes over the same temperature range (Figure 10A). The dynamic response test further confirmed its superiority compared to the (RT.pH13)-based sensor, showcasing its thermal stability, as illustrated in Figure 10B. Throughout these tests, a constant RH level of 10% was maintained. While the sensors exhibited responsivity to both decreasing and increasing temperatures within the specified range (i.e., 20 °C to −20 °C and 110 °C to 180 °C), the observed behavior could be attributed to the interplay of various factors, including the material properties of ZnO/Gt/PS. The calcination process likely enhanced the sensor's stability and reduced its response to temperature changes, resulting in a more consistent behavior.

During the evaluation with changing RH, as depicted in Figure 10C, the (RT.pH13)-based sensor manifested an increase in electrical resistance between 60% and 90% RH levels. This increase was then reversible upon dehumidification from 90% to 60%. In comparison,

the (RT.pH13.C)-based sensor demonstrated a notably lower increase in electrical resistance at the same RH ranges and enhanced stability with humidity fluctuations.

The behavior of the (RT.pH13)-based sensor implies that chemisorption processes, particularly chemical bonding between water molecules and the sensor's thin film, contribute to the observed rise in electrical resistance. The partial recovery of the initial resistance suggests that these chemisorption processes are not entirely reversible. On the contrary, the (RT.pH13.C)-based sensor exhibited a more stable and reversible response to humidity changes, indicating the dominance of physisorption processes where weaker forces, such as van der Waals interactions, hold water molecules. Overall, the calcination process is a crucial factor in improving the stability and reliability of sensors against both temperature and humidity by effectively eliminating residual organic impurities from the fabricated ZnO NPs. This improvement makes them more suitable for practical applications where consistent and reversible responses are paramount.

Exploring the sensors' mechanical properties is significant, particularly for applications intended for flexible sensors. These sensors must exhibit key characteristics, including flexibility and mechanical stability. The (RT. pH13)-based sensor's mechanical flexibility evaluation was started by determining the critical angle under ambient conditions (RT and RH ≈ 30–40%) at which the sensor would encounter electrical failure. As depicted in Figure 11A, the sensor's electrical resistance gradually increased to 45% at a bending angle of 90°.

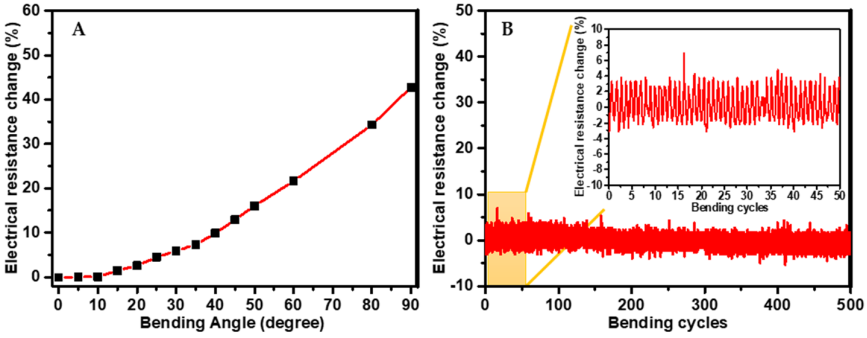

Figure 11. (**A**) Evaluation of critical bending angle for (RT. pH13)-based sensor's mechanical flexibility. (**B**) The sensor's mechanical flexibility assessed through repetitive bending at a bending angle 30°.

In previous work, we verified the exceptional mechanical flexibility of bare carbon electrodes, demonstrating minimal resistance changes under similar conditions [71–73]. This finding underscores that the observed alteration in electrical resistance primarily originated from the distortion and twisting of the sensing layer rather than the carbon electrode itself. Subsequently, the sensor's flexibility underwent further evaluation through repeated bending cycles at a chosen angle of 30° (bending radius ~ 1 cm). The sensor displayed robustness and stability, with no significant change in resistance (5%) even after undergoing hundreds of bending cycles at a bending angle of 30°, as illustrated in Figure 11B.

4. Conclusions

This study delves into the synthesis of ZnO NPs and their application in developing flexible gas sensors, providing a holistic exploration from NM synthesis to sensor performance. RT synthesis of ZnO NPs, particularly at a high basicity solution (pH ≈ 13), emerges as an efficient alternative to the hydrothermal method (hyd.C), obviating the need for intensive, costly, and time-consuming calcination. Eliminating the calcination step streamlines the overall synthesis procedure and contributes to a more sustainable and economical nanomaterial synthesis process, offering practical advantages for research and industrial applications.

The synthesized ZnO NPs (RT.pH13) exhibit commendable characteristics, including well-crystalline NPs with high thermal stability, as evidenced by minimal weight loss

(4.2 wt%) due to the effective removal of organic residues. These NPs exhibit a narrow particle size distribution (100–360 nm), bandgap of 3.0 eV consistent with that in the literature, and specific surface area of 14 m^2 g^{-1}, collectively positioning them as promising candidates for gas sensing applications. The elimination of the calcination step enhances the practicality and cost-effectiveness of the synthesis process, emphasizing the potential impact of these ZnO NPs in advancing flexible gas sensor technology.

Incorporating pre- and post-calcinated RT.pH13 NPs into flexible sensors showcases their versatility for gas detection at ambient conditions without the constraints of high operating temperatures, addressing challenges associated with traditional ZnO-based gas sensors. The investigation into gas sensing mechanisms underscores the influence of surface properties on sensor specificity and response to diverse gases, emphasizing the impact of calcination. In contrast, the (RT.pH13)-based sensor successfully detected $C_2H_4O_2$, C_8H_8, and $C_{10}H_{18}O$ gases. The (RT.pH13.C)-based sensor demonstrated lower responses in detecting the earlier-mentioned gases, but heightened sensitivity to C_6H_6, C_3H_6O, and C_2H_5OH gases. The study further explores the sensors' responses to temperature and humidity variations, revealing enhanced stability for the (RT.pH13.C)-based sensor attributed to removing the organic residues. These sensors' exceptional mechanical flexibility positions them as promising candidates for flexible and IoT applications. This research contributes to bridging the gap between ZnO NPs synthesis and application and paves the way for flexible gas sensor technology advancements.

Supplementary Materials: The following Supporting Information can be downloaded at https://www.mdpi.com/article/10.3390/chemosensors12050083/s1, Figure S1. The Nextron microprobe station with a Peltier-type sample stage. Figure S2 highlights the response to an 80 ppm C_8H_8 gas concentration, providing insights into the response and recovery times. Figure S3: TGA thermograms of raw PS, and PS films cured at 60 °C and 180 °C. Table S1: Literature overview of recent ZnO NMs employed in the development of gas sensors; Table S2: Literature overview of recent procedures to synthesize ZnONMs. References [25,38,74,83,101–122] are cited in the Supplementary Materials.

Author Contributions: Conceptualization, A.A.S. and R.I.; Methodology, F.M., A.A.S., M.O.B., H.A., M.K., and R.I.; Software, H.A. and M.K.; Validation, F.M., A.A.S., M.O.B., H.A., M.K., and R.I.; Formal analysis, F.M., A.A.S., M.O.B., H.A., and M.K.; Investigation, F.M., A.A.S., M.O.B., H.A., M.K., and R.I.; Resources, A.A.S. and R.I.; Data curation, F.M., A.A.S., M.O.B., and H.A.; Writing—original draft, F.M. and A.A.S.; Writing—review and editing, F.M., A.A.S., M.O.B., H.A., M.K., and R.I.; Visualization, F.M., A.A.S., H.A., and R.I.; Supervision, A.A.S., M.O.B., and R.I.; Project administration, A.A.S. and R.I.; Funding acquisition, R.I. All authors have read and agreed to the published version of the manuscript.

Funding: This research was funded by the Natural Sciences and Engineering Research Council of Canada (NSERC), grant number RGPIN-2023-05211, and MITACS, Canada, grant number IT31938.

Institutional Review Board Statement: Not applicable. This research did not involve humans or animals.

Informed Consent Statement: Not applicable for studies not involving humans.

Data Availability Statement: The research data are available upon request.

Acknowledgments: The authors are grateful for the generous funding support provided by the Natural Sciences and Engineering Research Council of Canada (NSERC) and MITACS, Canada, which made this research possible. Additionally, the authors would like to acknowledge the invaluable support and resources provided by the Research centers of NanoQAM (Centre de Recherche sur les Nanomateriaux et l'Énergie), LACIME (Laboratoire de communications et d'intégration de la microélectronique), and RESMIQ (Regroupement stratégique en microsystèmes du Québec). Their contributions were instrumental in the successful completion of this study.

Conflicts of Interest: The authors affirm that there are no conflicts of interest to disclose, both with the manuscript and concerning the company of Nextron microprobe station.

References

1. Weintraub, B.; Zhou, Z.; Li, Y.; Deng, Y. Solution Synthesis of One-Dimensional ZnO Nanomaterials and Their Applications. *Nanoscale* **2010**, *2*, 1573–1587. [CrossRef]
2. Subhan, M.A.; Neogi, N.; Choudhury, K.P. Industrial Manufacturing Applications of Zinc Oxide Nanomaterials: A Comprehensive Study. *Nanomanufacturing* **2022**, *2*, 265–291. [CrossRef]
3. Chaudhary, S.; Umar, A.; Bhasin, K.; Baskoutas, S. Chemical Sensing Applications of ZnO Nanomaterials. *Materials* **2018**, *11*, 287. [CrossRef]
4. Nguyen, N.-K.; Nguyen, T.; Nguyen, T.-K.; Yadav, S.; Dinh, T.; Masud, M.K.; Singha, P.; Do, T.N.; Barton, M.J.; Ta, H.T.; et al. Wide-Band-Gap Semiconductors for Biointegrated Electronics: Recent Advances and Future Directions. *ACS Appl. Electron. Mater.* **2021**, *3*, 1959–1981. [CrossRef]
5. Papadimitriou, D.N. Engineering of Optical and Electrical Properties of Electrodeposited Highly Doped Al:ZnO and In:ZnO for Cost-Effective Photovoltaic Device Technology. *Micromachines* **2022**, *13*, 1966. [CrossRef]
6. Zhang, L.; Li, N.; Ma, Q.; Ding, J.; Chen, C.; Hu, Z.; Zhao, W.; Li, Y.; Feng, H.; Li, M.; et al. Large-Area Flexible and Transparent UV Photodetector Based on Cross-Linked AgNW@ZnONRs with High Performance. *J. Mater. Sci. Technol.* **2022**, *110*, 65–72. [CrossRef]
7. Du, B.; Zhang, M.; Ye, J.; Wang, D.; Han, J.; Zhang, T. Novel Au Nanoparticle-Modified ZnO Nanorod Arrays for Enhanced Photoluminescence-Based Optical Sensing of Oxygen. *Sensors* **2023**, *23*, 2886. [CrossRef]
8. Gatou, M.-A.; Lagopati, N.; Vagena, I.-A.; Gazouli, M.; Pavlatou, E.A. ZnO Nanoparticles from Different Precursors and Their Photocatalytic Potential for Biomedical Use. *Nanomaterials* **2022**, *13*, 122. [CrossRef]
9. Al-Arjan, W.S. Zinc Oxide Nanoparticles and Their Applicationin Adsorption of Toxic Dye from Aqueous Solution. *Polymers* **2022**, *14*, 3086. [CrossRef]
10. Ananthi, S.; Kavitha, M.; Kumar, E.R.; Prakash, T.; Poonguzhali, R.V.; Ranjithkumar, B.; Balamurugan, A.; Srinivas, C.; Sastry, D. Investigation of Physicochemical Properties of ZnO Nanoparticles for Gas Sensor Applications. *Inorg. Chem. Commun.* **2022**, *146*, 110152. [CrossRef]
11. Shin, K.Y.; Mirzaei, A.; Oum, W.; Yu, D.J.; Kang, S.; Kim, E.B.; Kim, H.M.; Kim, S.S.; Kim, H.W. Enhancement of SelectiveNO_2 Gas Sensing via Xenon Ion Irradiation of ZnO Nanoparticles. *Sens. Actuators B Chem.* **2023**, *374*, 132808. [CrossRef]
12. Raha, S.; Ahmaruzzaman, M. ZnO Nanostructured Materials and Their Potential Applications: Progress, Challenges and Perspectives. *Nanoscale Adv.* **2022**, *4*, 1868–1925. [CrossRef]
13. Sulaiman, S.; Izman, S.; Uday, M.; Omar, M. Review on Grain Size Effects on Thermal Conductivity in ZnO Thermoelectric Materials. *RSC Adv.* **2022**, *12*, 5428–5438. [CrossRef]
14. Patil, S.A.; Jagdale, P.B.; Singh, A.; Singh, R.V.; Khan, Z.; Samal, A.K.; Saxena, M. 2D Zinc Oxide–Synthesis, Methodologies, Reaction Mechanism, and Applications. *Small* **2023**, *19*, 2206063. [CrossRef] [PubMed]
15. Preeti, K.; Kumar, A.; Jain, N.; Kaushik, A.; Mishra, Y.K.; Sharma, S.K. Tailored ZnO Nanostructures for Efficient Sensing of Toxic Metallic Ions of Drainage Systems. *Mater. Today Sustain.* **2023**, *24*, 100515. [CrossRef]
16. Yadav, M.; Kumar, M.; Chaudhary, S.; Yadav, K.; Sharma, A. A Review on Chemiresistive Hybrid Zinc Oxide and Nanocomposites for Gas Sensing. *Ind. Eng. Chem. Res.* **2023**, *62*, 11259–11278. [CrossRef]
17. Saleh, T.A.; Fadillah, G. Green Synthesis Protocols, Toxicity, and Recent Progressin Nanomaterial-Based for Environmental Chemical Sensors Applications. *Trends Environ. Anal. Chem.* **2023**, *39*, e00204. [CrossRef]
18. Won, D.; Bang, J.; Choi, S.H.; Pyun, K.R.; Jeong, S.; Lee, Y.; Ko, S.H. Transparent Electronics for Wearable Electronics Application. *Chem. Rev.* **2023**, *123*, 9982–10078. [CrossRef]
19. Kurugundla, G.K.; Godavarti, U.; Saidireddy, P.; Pothukanuri, N. Zinc Oxide Based Gas Sensors and Their Derivatives: A Critical Review. *J. Mater. Chem. C* **2023**, *11*, 3906–3925. [CrossRef]
20. Kumar, R.; Al-Dossary, O.; Kumar, G.; Umar, A. Zinc Oxide Nanostructures for NO_2 Gas–Sensor Applications: A Review. *Nano-Micro Lett.* **2015**, *7*, 97–120. [CrossRef]
21. To, D.T.H.; Park, J.Y.; Yang, B.; Myung, N.V.; Choa, Y.-H. Nanocrystalline ZnO Quantum Dot-Based Chemiresistive Gas Sensors: Improving Sensing Performance towards NO_2 and H_2S by Optimizing Operating Temperature. *Sens. Actuators Rep.* **2023**, *6*, 100166. [CrossRef]
22. Ramike, M.P.; Ndungu, P.G.; Mamo, M.A. Exploration of the Different Dimensions of Wurtzite ZnO Structure Nanomaterial sas Gas Sensors at Room Temperature. *Nanomaterials* **2023**, *13*, 2810. [CrossRef] [PubMed]
23. Cai, Z.; Park, J.; Park, S. Synthesis of Flower-like ZnO and Its Enhanced Sensitivity towards NO_2 Gas Detection at Room Temperature. *Chemosensors* **2023**, *11*, 322. [CrossRef]
24. Zeng, T.; Ma, D.; Gui, Y. Gas-Sensitive Performance Study of Metal (Au,Pd,Pt)/ZnO Heterojunction Gas Sensors for Dissolved Gases in Transformer Oil. *Langmuir* **2024**, *40*, 9819–9830. [CrossRef] [PubMed]
25. Li, Y.; Zhang, B.; Li, J.; Duan, Z.; Yang, Y.; Yuan, Z.; Jiang, Y.; Tai, H. Pd-Decorated ZnO Hexagonal Microdiscs for NH_3 Sensor. *Chemosensors* **2024**, *12*, 43. [CrossRef]
26. Alouani, M.A.; Casanova-Cháfer, J.; Güell, F.; Peña-Martín, E.; Ruiz-Martínez-Al Cocer, S.; de Bernardi-Martín, S.; García-Gómez, A.; Vilanova, X.; Llobet, E. ZnO-Loaded Graphene for NO_2 Gas Sensing. *Sensors* **2023**, *23*, 6055. [CrossRef] [PubMed]
27. Wang, T.; Chen, J.; Chen, J.; Yao, X.; Chen, G.; Jiao, Z.; Zhao, J.-T.; Cheng, S.; Yang, X.-C.; Li, Q. UV-Light Enhanced Gas Sensor Based on Ga Doped ZnO for Ultra-High Sensitive and Selective n-Butanol Detection. *Appl. Surf. Sci.* **2023**, *641*, 158551. [CrossRef]

28. Ou, L.-X.; Liu, M.-Y.; Zhu, L.-Y.; Zhang, D.W.; Lu, H.-L. Recent Progress on Flexible Room-Temperature Gas Sensors Based on Metal Oxide Semiconductor. *Nano-Micro Lett.* **2022**, *14*, 206. [CrossRef]
29. Güell, F.; Galdámez-Martínez, A.; Martinez-Alanis, P.R.; Catto, A.C.; da Silva, L.F.; Mastelaro, V.R.; Santana, G.; na Dutt, A. ZnO-Based Nanomaterials Approach for Photocatalytic and Sensing Applications: Recent Progress and Trends. *Mater. Adv.* **2023**, *4*, 3685–3707. [CrossRef]
30. Wawrzyniak, J. Advancements in Improving Selectivity of Metal Oxide Semiconductor Gas Sensors Opening New Perspectives for Their Application in Food Industry. *Sensors* **2023**, *23*, 9548. [CrossRef]
31. GaneshMoorthy, S.; Bouvet, M. Effects of Visible Lighton Gas Sensors: From Inorganic Resistors to Molecular Material-Based Heterojunctions. *Sensors* **2024**, *24*, 1571. [CrossRef] [PubMed]
32. Pineda-Reyes, A.M.; Herrera-Rivera, M.R.; Rojas-Chávez, H.; Cruz-Martínez, H.; Medina, D.I. Recent Advances in ZnO-Based Carbon Monoxide Sensors: Role of Doping. *Sensors* **2021**, *21*, 4425. [CrossRef]
33. Abdelkarem, K.; Saad, R.; ElSayed, A.M.; Fathy, M.; Shaban, M.; Hamdy, H. Design of High-Sensitivity La-Doped ZnO Sensors for CO_2 Gas Detection at Room Temperature. *Sci. Rep.* **2023**, *13*, 18398. [CrossRef] [PubMed]
34. Wang, L.; Choi, J. Improved Recovery of NO_2 Sensors Using Heterojunctions between Transition Metal Dichalcogenides and ZnO Nanoparticles. *Micro Nano Syst. Lett.* **2023**, *11*, 5. [CrossRef]
35. Hjiri, M.; Algessair, S.; Dhahri, R.; Albargi, H.B.; Mansour, N.B.; Assadi, A.; Neri, G. Ammonia Gas Sensors Based on Undoped and Ca-Doped ZnO Nanoparticles. *RSC Adv.* **2024**, *14*, 5001–5011. [CrossRef] [PubMed]
36. Xu, H.; Gong, Z.-X.; Huo, L.-Z.; Guo, C.-F.; Yang, X.-J.; Wang, Y.-X.; Luo, X.-P. Zinc Oxide-Loaded Cellulose-Based Carbon Gas Sensor for Selective Detection of Ammonia. *Nanomaterials* **2023**, *13*, 3151. [CrossRef] [PubMed]
37. Ahmad, I.A.; Mohammed, Y.H. Synthesis of ZnO Nanowires by Thermal Chemical Vapor Deposition Technique: Role of Oxygen Flow Rate. *Micro Nanostruct.* **2023**, *181*, 207628. [CrossRef]
38. Torres, F.D.C.G.; López, J.L.C.; Rodríguez, A.S.L.; Gallardo, P.S.; Morales, E.R.; Hernández, G.P.; Guillen, J.C.D.; Flores, L.L.D. Sol–Gel/Hydrothermal Synthesis of Well-Aligned ZnO Nanorods. *Bol. Soc. Esp. Ceram. Vidr.* **2023**, *62*, 348–356. [CrossRef]
39. Khoshsang, H.; Abbasi, K.; Ghaffarinejad, A. Biosynthesis of ZnO and CuO Nanoparticles Using Sun flower Petal Extract. *Inorg. Chem. Commun.* **2023**, *155*, 111083. [CrossRef]
40. Juwono, H.; Zakiyah, A.; Subagyo, R.; Kusumawati, Y. Facile Production of Biodiesel from Candlenut Oil (*Aleurites moluccana* L.) Using Photocatalytic Method by Nano Sized-ZnO Photocatalytic Agent Synthesized via Polyol Method. *Indones. J. Chem.* **2023**, *23*, 1304–1314. [CrossRef]
41. Zheng, A.; Abdullah, C.; Chung, E.; Andou, Y. Recent Progress in Visible Light-Doped ZnO Photocatalyst for Pollution Control. *Int. J. Environ. Sci. Technol.* **2023**, *20*, 5753–5772. [CrossRef]
42. Baladi, M.; Amiri, M.; Mohammadi, P.; Mahdi, K.S.; Golshani, Z.; Razavi, R.; Salavati-Niasari, M. Green Sol–Gel Synthesis of Hydroxyapatite Nanoparticles Using Lemon Extractas Capping Agent and Investigation of Its Anticancer Activity against Human Cancer Cell Lines (T98, and SHSY5). *Arab. J. Chem.* **2023**, *16*, 104646. [CrossRef]
43. Aldeen, T.S.; Mohamed, H.E.A.; Maaza, M. ZnO Nanoparticles Prepared via a Green Synthesis Approach: Physical Properties, Photocatalytic and Antibacterial Activity. *J. Phys. Chem. Solids* **2022**, *160*, 110313. [CrossRef]
44. Mohammad, M.; Malek, M.F.; AbdHalim, M.F.; Mohammad Zamri, N.Z.; Bakri, M.D.; Khusaimi, Z.; Mamat, M.H.; Mahmood, M.R.; Tetsuo, S. Synthesisation of Zinc Oxide Nanowires via Hybrid Microwave Assisted Sonochemical Technique at Various Microwave Power. *J. Mech. Eng.* **2023**, *20*, 293–311. [CrossRef]
45. Chen, Y.; Li, H.; Huang, D.; Wang, X.; Wang, Y.; Wang, W.; Yi, M.; Cheng, Q.; Song, Y.; Han, G. Highly Sensitive and Selective Acetone Gas Sensors Based on Modified ZnO Nanomaterials. *Mater. Sci. Semicond. Process.* **2022**, *148*, 106807. [CrossRef]
46. Xu, J.; Huang, Y.; Zhu, S.; Abbes, N.; Jing, X.; Zhang, L. A Review of the Green Synthesis of ZnO Nanoparticles Using Plant Extracts and Their Prospects for Application in Antibacterial Textiles. *J. Eng. Fibers. Fab.* **2021**, *16*, 15589250211046242. [CrossRef]
47. Almarhoon, Z.M.; Indumathi, T.; Kumar, E.R. Optimized Green Synthesis of ZnO Nanoparticles: Evaluation of Structural, Morphological, Vibrational and Optical Properties. *J. Mater. Sci. Mater. Electron.* **2022**, *33*, 23659–23672. [CrossRef]
48. Sharma, B.K.; Mehta, B.R.; Shah, E.V.; Chaudhari, V.P.; Roy, D.R.; MondalRoy, S. Green Synthesis of Triangular ZnO Nanoparticles Using *Azadirachta indica* Leaf Extract and Its Shape Dependency for Significant Antimicrobial Activity: Joint Experimental and Theoretical Investigation. *J. Clust. Sci.* **2022**, *33*, 2517–2530. [CrossRef]
49. Sanjeev, N.O.; Valsan, A.E.; Zachariah, S.; Vasu, S.T. Synthesis of Zinc Oxide Nanoparticles from *Azadirachta indica* Extract: A Sustainable and Cost-Effective Material for Waste water Treatment. *J. Hazard. Toxic Radioact. Waste* **2023**, *27*, 04023027. [CrossRef]
50. Ferreiro, A.; Flores-Carrasco, G.; Quevedo-López, M.; Urbieta, A.; Fernández, P.; Rabanal, M. Effect of Lithium Codoping on the Structural, Morphological and Photocatalytic Properties of Nd-Doped ZnO. *Ceram. Int.* **2023**, *49*, 33513–33524. [CrossRef]
51. Reyes-Gracia, A.; Alvarado, J.A.; Pérez-Cuapio, R.; Juárez, H. Comparison from Lemon Juice and N-Dipentene ZnO Nanoparticles Green Synthesis: Influence of By products in Morphology and Size. *Mater. Sci. Eng. B* **2023**, *290*, 116335. [CrossRef]
52. Khnam, B.R.; Prachalith, N.; Angadi, B.; Reddy, B.U.; Udaykumar, K. The Effect of Reaction and Annealing Temperatures on Physicochemical Properties of Highly Stable ZnO Nanoparticles Synthesized via a Green Route Using *Plumeria obtuse* L. *New J. Chem.* **2023**, *47*, 19122–19137. [CrossRef]
53. Narin, P.; Kutlu-Narin, E.; Lisesivdin, S.B. Growth Dynamics of Mist-CVD Grown ZnO Nanoplatelets. *Phys B Condens. Matter* **2021**, *614*, 413028. [CrossRef]

54. Pradeep, N.; selvi Gopal, T.; Venkatraman, U.; Alrebdi, T.A.; Pandiaraj, S.; Alodhayb, A.; Muthuramamoorthy, M.; Kim, S.Y.; Van Le, Q.; Khan, S.; et al. Effect of Substrate Bending towards Chemiresistive Based Hydrogen Gas Sensor Using ZnO-Decorated MgO Nanocubes. *Mater. Today Chem.* **2022**, *26*, 101200. [CrossRef]
55. Choi, S.C.; Lee, D.K.; Sohn, S.H. Morphological Properties of One-Dimensional ZnO Nanostructures Grown by Thermal Chemical Vapor Deposition with Defferent Source Materials. *Mol. Cryst. Liq. Cryst.* **2022**, *735*, 126–133. [CrossRef]
56. Nisansala, H.; Rajapaksha, G.; Dikella, D.; Dheerasinghe, M.; Sirimuthu, N.; Patabendige, C. Zinc Oxide Nanostructures in the Textile Industry. *Indian J. Sci. Technol.* **2021**, *14*, 3370–3395. [CrossRef]
57. Li, S.-M.; Zhang, L.-X.; Zhu, M.-Y.; Ji, G.-J.; Zhao, L.-X.; Yin, J.; Bie, L.-J. Acetone Sensing of ZnO Nanosheets Synthesized Using Room-Temperature Precipitation. *Sens. Actuators B Chem.* **2017**, *249*, 611–623. [CrossRef]
58. Malik, K.A.; Malik, J.H.; Assadullah, I.; Bhat, A.A.; Tomar, R. A Comparative Experimental and Theoretical Study on the Structural and Optical Properties of ZnO Synthesized at Room Temperature Using an Ultrasonication Technique. *Energy Storage* **2023**, *5*, e401. [CrossRef]
59. Arya, S.; Mahajan, P.; Mahajan, S.; Khosla, A.; Datt, R.; Gupta, V.; Young, S.-J.; Oruganti, S.K. Influence of Processing Parameters to Control Morphology and Optical Properties of Sol-Gel Synthesized ZnO Nanoparticles. *ECS J. Solid State Sci. Technol.* **2021**, *10*, 023002. [CrossRef]
60. Shaba, E.Y.; Jacob, J.O.; Tijani, J.O.; Suleiman, M.A.T. A Critical Review of Synthesis Parameters Affecting the Properties of Zinc Oxide Nanoparticle and Its Application in Wastewater Treatment. *Appl. Water Sci.* **2021**, *11*, 48. [CrossRef]
61. Endriyatno, N.; Wikantyasning, E.; Indrayudha, P. Optimization synthesis of zinc oxide nanoparticles using factorial design and its antibacterial activity. *Rasayan J. Chem.* **2023**, *16*, 773–778. [CrossRef]
62. Arif, H.; Qayyum, S.; Akhtar, W.; Fatima, I.; Kayani, W.K.; Rahman, K.U.; Al-Onazi, W.A.; Al-Mohaimeed, A.M.; Bangash, N.K.; Ashraf, N.; et al. Synthesis and Characterization of Zinc Oxide Nanoparticles at Different pH Values from *Clinopodiumvulgare* L. and Their Assessment as an Antimicrobial Agent and Biomedical Application. *Micromachines* **2023**, *14*, 1285. [CrossRef] [PubMed]
63. Sheikhi, S.; Aliannezhadi, M.; Tehrani, F.S. Effect of Precursor Material, pH, and Aging on ZnO Nanoparticles Synthesized by One-Step Sol–Gel Method for Photodynamic and Photocatalytic Applications. *Eur. Phys. J. Plus* **2022**, *137*, 60. [CrossRef]
64. Gherbi, B.; Laouini, S.E.; Meneceur, S.; Bouafia, A.; Hemmami, H.; Tedjani, M.L.; Thiripuranathar, G.; Barhoum, A.; Menaa, F. Effect of pH Value on the Bandgap Energy and Particles Size for Biosynthesis of ZnO Nanoparticles: Efficiency for Photocatalytic Adsorption of Methyl Orange. *Sustainability* **2022**, *14*, 11300. [CrossRef]
65. Ali, A.; Yusoff, M.; TerTeo, P.; Mamat, S.; Mohamed, M.; Ramli, N.; Akmal, S. Synthesis of Zinc Oxide Nanostructures Growth by the Role of pH Variation. *IOP Conf. Series Earth Environ. Sci.* **2020**, *596*, 012040. [CrossRef]
66. Devi, L.R.; Sarathi, R.; Sheeba, N.; Esakki, E.S.; Sundar, S.M. Influence of pH Variation on Structural, Optical, and Super-paramagnetic Behavior of Ni-Doped ZnO (X=0.02) Using a Solvothermal Method. *J. Indian Chem. Soc.* **2023**, *100*, 100874. [CrossRef]
67. Kumar, S.; Ye, F.; Mazinani, B.; Dobretsov, S.; Dutta, J. Chitosan Nanocomposite Coatings Containing Chemically Resistant ZnO–SnOx Core–Shell Nanoparticles for Photocatalytic Antifouling. *Int. J. Mol. Sci.* **2021**, *22*, 4513. [CrossRef] [PubMed]
68. Gerbreders, V.; Krasovska, M.; Sledevskis, E.; Gerbreders, A.; Mihailova, I.; Tamanis, E.; Ogurcovs, A. Hydrothermal Synthesis of ZnO Nanostructures with Controllable Morphology Change. *Cryst. Eng. Comm.* **2020**, *22*, 1346–1358. [CrossRef]
69. Du, H.; Yue, M.; Huang, X.; Duan, G.; Yang, Z.; Huang, W.; Shen, W.; Yin, X. Preparation, Application and Enhancement Dyeing Properties of ZnO Nanoparticles in Silk Fabrics Dyed with Natural Dyes. *Nanomaterials* **2022**, *12*, 3953. [CrossRef]
70. Kedruk, Y.; Baigarinova, G.; Gritsenko, L.; Cicero, G.; Abdullin, K.A. Facile Low-Cost Synthesis of Highly Photocatalitycally Active Zinc Oxide Powders. *Front. Mater.* **2022**, *9*, 869493. [CrossRef]
71. Al Shboul, A.M.; Izquierdo, R. Printed Chemiresistive In_2O_3 Nanoparticle-Based Sensors with Ppb Detection of H_2S Gas for Food Packaging. *ACS Appl. Nano Mater.* **2021**, *4*, 9508–9517. [CrossRef]
72. Al Shboul, A.; Shih, A.; Izquierdo, R. A Flexible Indium Oxide Sensor with Anti-Humidity Property for Room Temperature Detection of Hydrogen Sulfide. *IEEE Sens. J.* **2020**, *21*, 9667–9674. [CrossRef]
73. Al Shboul, A.M.; Ketabi, M.; Mechael, S.S.; Nyayachavadi, A.; Rondeau-Gagné, S.; Izquierdo, R. Hydrogen Sulfide Gas Detection in Ppb Levels at Room Temperature with a Printed, Flexible, Disposable In_2O_3 NPs-Based Sensor for IoT Food Packaging Applications. *Adv. Mater. Technol.* **2023**, *8*, 2201086. [CrossRef]
74. Nextron. Available online: https://www.microprobesystem.com (accessed on 2 May 2024).
75. Rajendran, G.; Datta, S.P.; Singh, R.D.; Datta, S.C.; Vakada, M. Synthesisand Characterization of ZnO Nanoparticles–Comparison of Acetate (Precursor) Based Methods. *Inorg. Nano-Met. Chem.* **2022**, *52*, 185–194. [CrossRef]
76. Jum'h, I.; Telfah, A.; Lambert, J.; Gogiashvili, M.; Al-Taani, H.; Hergenröder, R. 13C and 1H NMR Measurements to Investigate the Kinetics and the Mechanism of Acetic Acid (CH_3CO_2H) Ionization as a Model for Organic Acid Dissociation Dynamics for Polymeric Membrane Water Filtration. *J. Mol. Liq.* **2017**, *227*, 106–113. [CrossRef]
77. Syrovaya, A.; Levashova, O.; Chalenko, N.; Petyunina, V.; Makarov, V.; Andreeva, S.; Lukianova, L.; Kozub, S.; Tishakova, T.; Savelieva, E.; et al. *Acid-Base Equilibrium in the Organism. pH of Biological Liquids*; KhNMU Medical Chemistry: Kharkiv, Ukraine, 2017; p. 24.
78. Liu, W.; Wang, S.; Wang, J.; Zhang, B.; Liu, L.; Liu, H.; Yang, J. Super critical Hydrothermal Synthesis of Nano-Zinc Oxide: Process and Mechanism. *Ceram. Int.* **2022**, *48*, 22629–22646. [CrossRef]

79. Droepenu, E.K.; Wee, B.S.; Chin, S.F.; Kok, K.Y.; Maligan, M.F. Zinc Oxide Nanoparticles Synthesis Methods and Its Effecton Morphology: A Review. *Biointerface Res. Appl. Chem.* **2022**, *12*, 4261–4292. [CrossRef]
80. Lausecker, C.; Salem, B.; Baillin, X.; Consonni, V. Effects of Zinc Nitrate and HMTA on the Formation Mechanisms of ZnO Nanowires on Au Seed Layers. *Cryst. Growth. Des.* **2023**, *23*, 2941–2950. [CrossRef]
81. Gatou, M.-A.; Kontoliou, K.; Volla, E.; Karachalios, K.; Raptopoulos, G.; Paraskevopoulou, P.; Lagopati, N.; Pavlatou, E.A. Optimization of ZnO Nanoparticles' Synthesis via Precipitation Method Applying Taguchi Robust Design. *Catalysts* **2023**, *13*, 1367. [CrossRef]
82. Bulcha, B.; Leta Tesfaye, J.; Anatol, D.; Shanmugam, R.; Dwarampudi, L.P.; Nagaprasad, N.; Bhargavi, V.N.; Krishnaraj, R. Synthesis of Zinc Oxide Nanoparticles by Hydrothermal Methods and Spectroscopic Investigation of Ultraviolet Radiation Protective Properties. *J. Nanomater.* **2021**, *2021*, 8617290. [CrossRef]
83. Batterjee, M.G.; Nabi, A.; Kamli, M.R.; Alzahrani, K.A.; Danish, E.Y.; Malik, M.A. Green Hydrothermal Synthesis of Zinc Oxide Nanoparticles for UV-Light-Induced Photocatalytic Degradation of Ciprofloxacin Antibiotic in an Aqueous Environment. *Catalysts* **2022**, *12*, 1347. [CrossRef]
84. Erol, I.; Hazman, Ö.; Aksu, M. Preparation of Novel Composites of Polyvinyl Alcohol Containing Hesperidin Loaded ZnO Nanoparticles and Determination of Their Biological and Thermal Properties. *J. Inorg. Organomet. Poly. Mater.* **2023**, *33*, 731–746. [CrossRef] [PubMed]
85. Wahab, R.; Ansari, S.; Kim, Y.-S.; Seo, H.-K.; Shin, H.-S. Room Temperature Synthesis of Needle-Shaped ZnO Nanorods via Sonochemical Method. *Appl. Surf. Sci.* **2007**, *253*, 7622–7626. [CrossRef]
86. Aydoğdu, N.K.S.B. Comparison of ZnO Nanoparts Synthesized with *Vitisvinifera* L. Cv. Öküzgözüby Thermogravimetric Analysis (TGA) According to Drying Temperatures. In Proceedings of the 17th Nanoscience and Nanotechnology Conference, Izmir-Urla, Izmir-Urla, Turkey, 27–30 August 2023.
87. Limón-Rocha, I.; Guzmán-González, C.A.; Anaya-Esparza, L.M.; Romero-Toledo, R.; Rico, J.L.; González-Vargas, O.A.; Pérez-Larios, A. Effect of the Precursor on the Synthesis of ZnO and Its Photocatalytic Activity. *Inorganics* **2022**, *10*, 16. [CrossRef]
88. Ramesh, A.M.; Pal, K.; Kodandaram, A.; Manjula, B.L.; Ravishankar, D.K.; Gowtham, H.G.; Murali, M.; Rahdar, A.; Kyzas, G.Z. Antioxidant and Photocatalytic Properties of Zinc Oxide Nanoparticles Phyto-Fabricated Using the Aqueous Leaf Extract of Sida Acuta. *Green Process. Synth.* **2022**, *11*, 857–867. [CrossRef]
89. Sajid, M.M.; Shad, N.A.; Javed, Y.; Shafique, M.; Afzal, A.M.; Khan, S.B.; Amin, N.; Hassan, M.A.; Khan, M.U.H.; Tarabi, T.; et al. Efficient Photocatalytic and Antimicrobial Behaviour of Zinc Oxide Nanoplates Prepared by Hydrothermal Method. *J. Clust. Sci.* **2022**, *33*, 773–783. [CrossRef]
90. Gonzalez, E.D.; Ospina, R.; Gonzalez-Estrada, O.A.; Botero, J.; Botero, M.A. Influence of the Filling Ratio of Vial in Chemical Surface and Physicochemical Properties of ZnO Nanoparticles Obtained by Planetary Ball Milling Process. *Surf. Interface Anal.* **2023**, *55*, 263–269. [CrossRef]
91. Singh, K.; Nancy; Bhattu, M.; Singh, G.; Mubarak, N.M.; Singh, J. Light-Absorption-Driven Photocatalysis and Antimicrobial Potential of PVP-Capped ZincOxide Nanoparticles. *Sci. Rep.* **2023**, *13*, 13886. [CrossRef]
92. Alzahrani, E.A.; Nabi, A.; Kamli, M.R.; Albukhari, S.M.; Althabaiti, S.A.; Al-Harbi, S.A.; Khan, I.; Malik, M.A. Facile Green Synthesis of ZnO NPs and Plasmonic Ag-Supported ZnO Nanocomposite for Photocatalytic Degradation of Methylene Blue. *Water* **2023**, *15*, 384. [CrossRef]
93. El-Dawy, E.G.A.E.M.; Gherbawy, Y.A.; AbdEl-Sadek, M.S.; Fouad, W. Molecular Identification of Keratinophilic Fungi Associated with Hair Scalp and Antifungal Activity of Green-Synthesis Zinc Oxide Nanoparticles. *J. Basic. Microbiol.* **2023**, *64*, e2300447. [CrossRef]
94. Franco, M.A.; Conti, P.P.; Andre, R.S.; Correa, D.S. A Review on Chemiresistive ZnO Gas Sensors. *Sens. Actuators Rep.* **2022**, *4*, 100100. [CrossRef]
95. Kang, Y.; Yu, F.; Zhang, L.; Wang, W.; Chen, L.; Li, Y. Review of ZnO-Based Nanomaterials in Ga Sensors. *Solid State Ion.* **2021**, *360*, 115544. [CrossRef]
96. Kutilike, B.; Hamidin, T.; Nizamidin, P.; Abliz, S.; Yimit, A. Improved Determination of Styrene with a Titanium (IV) Oxide Film Optical Waveguide Doped with Zinc Ferrite. *Instrum. Sci. Technol.* **2020**, *49*, 216–232. [CrossRef]
97. Yang, J.; Ren, C.; Liu, M.; Li, W.; Gao, D.; Li, H.; Ning, Z. A Novel Dye-Modified Metal–Organic Framework as a Bifunctional Fluorescent Probe for Visual Sensing for Styrene and Temperature. *Molecules* **2023**, *28*, 4919. [CrossRef] [PubMed]
98. Liu, B.; Li, Y.; Gao, L.; Zhou, F.; Duan, G. Ultrafine Pt NPs-Decorated SnO_2/α-Fe_2O_3 Hollow Nanospheres with Highly Enhanced Sensing Performances for Styrene. *J. Hazard. Mater.* **2018**, *358*, 355–365. [CrossRef]
99. Mian, S.A.; Hussain, A.; Basit, A.; Rahman, G.; Ahmed, E.; Jang, J. Molecular Modeling and Simulation of Transition Metal–Doped Molybdenum Disulfide Biomarkers in Exhaled Gases for Early Detection of Lung Cancer. *J. Mol. Model.* **2023**, *29*, 225. [CrossRef] [PubMed]
100. Widjaja, E. Suspension Polymerization of Styrene Using Zinc Oxide as a Suspension Agent. *J. Mater. Sci. Eng. B* **2011**, *1*, 404.
101. Himabindu, B.; Latha Devi, N.S.M.P.; Nagaraju, P.; Rajini Kanth, B. A Nanostructured Al-Doped ZnO as an Ultra-Sensitive Room-Temperature Ammonia Gas Sensor. *J. Mater. Sci. Mater. Electron.* **2023**, *34*, 1014. [CrossRef]
102. Lupan, C.; Mishra, A.K.; Wolff, N.; Drewes, J.; Krüger, H.; Vahl, A.; Lupan, O.; Pauporté, T.; Viana, B.; Kienle, L.; et al. Nanosensors Based on a Single ZnO: Eu Nanowire for Hydrogen Gas Sensing. *ACS Appl. Mater. Interfaces* **2022**, *14*, 41196–41207. [CrossRef]

103. Liu, S.; Yang, W.; Liu, L.; Chen, H.; Liu, Y. Enhanced H2S Gas-Sensing Performance of Ni-Doped ZnO Nanowire Arrays. *ACS Omega* **2023**, *8*, 7595–7601. [CrossRef]
104. Lin, J.-H.; Yang, T.; Zhang, X.; Shiu, B.-C.; Lou, C.-W.; Li, T.-T. Mn-Doped ZnO/SnO_2-Based Yarn Sensor for Ammonia Detection. *Ceram. Int.* **2023**, *49*, 34431–34439. [CrossRef]
105. Daniel, T.T.; Yadav, V.K.S.; Abraham, E.E.; Paily, R.P. Carbon Monoxide Sensor Based on Printed ZnO. *IEEE Sens. J.* **2022**, *22*, 10910–10917. [CrossRef]
106. Tseng, S.-F.; Chen, P.-S.; Hsu, S.-H.; Hsiao, W.-T.; Peng, W.-J. Investigation of Fiber Laser-Induced Porous Graphene Electrodes in Controlled Atmospheres for ZnO Nanorod-Based NO_2 Gas Sensors. *Appl. Surf. Sci.* **2023**, *620*, 156847. [CrossRef]
107. Kamble, C.; Narwade, S.; Mane, R. Detection of Acetylene (C_2H_2) Gas Using Ag-Modified ZnO/GO Nanorods Prepared by a Hydrothermal Synthesis. *Mater. Sci. Semicond. Process.* **2023**, *153*, 107145. [CrossRef]
108. Kumar, B.B.; Bhowmik, B.; Singh, A.P.; Jit, S.; Singh, K. Room Temperature ZnO Nanorods Based TFT Ammonia Sensor: An Experimental and Simulation Study. *Appl. Phys. A* **2024**, *130*, 308. [CrossRef]
109. Chao, J.; Meng, D.; Zhang, K.; Wang, J.; Guo, L.; Yang, X. Development of an Innovative Ethanol Sensing Sensor Platform Based on the Construction of Au Modified 3D Porous ZnO Hollow Microspheres. *Mater. Res. Bull.* **2024**, *170*, 112569. [CrossRef]
110. Natarajamani, G.S.; Kannan, V.P.; Madanagurusamy, S. Synergistically Enhanced NH3 Gas Sensing of Graphene Oxide-Decorated Nano-ZnO Thin Films. *Mater. Chem. Phys.* **2024**, *316*, 129036. [CrossRef]
111. Bolli, E.; Fornari, A.; Bellucci, A.; Mastellone, M.; Valentini, V.; Mezzi, A.; Polini, R.; Santagata, A.; Trucchi, D.M. Room-Temperature O3 Detection: Zero-Bias Sensors Based on ZnO Thin Films. *Crystals* **2024**, *14*, 90. [CrossRef]
112. Kim, J.-Y.; Mirzaei, A.; Lee, M.H.; Kim, T.-U.; Kim, S.S.; Kim, J.-H. Boosting the Acetone Gas Sensing of WS2–ZnO Nanosheets by Codecoration of Pt/Pd Nanoparticles. *J. Alloys. Compd.* **2024**, *989*, 174325. [CrossRef]
113. Nguyena, N.; Nguyen, V. Ultrasound-Assisted Sol-Gel Synthesis, Characterization, and Photocatalytic Application of ZnO Nanoparticles. *Dig. J. Nanomater. Biostruct.* **2023**, *18*, 889–897. [CrossRef]
114. Haque, M.J.; Bellah, M.M.; Hassan, M.R.; Rahman, S. Synthesis of ZnO Nanoparticles by Two Different Methods & Comparison of Their Structural, Antibacterial, Photocatalytic and Optical Properties. *Nano Express* **2020**, *1*, 010007. [CrossRef]
115. Al Awadh, A.A.; Shet, A.R.; Patil, L.R.; Shaikh, I.A.; Alshahrani, M.M.; Nadaf, R.; Mahnashi, M.H.; Desai, S.V.; Muddapur, U.M.; Achappa, S.; et al. Sustainable Synthesis and Characterization of Zinc Oxide Nanoparticles Using Raphanus Sativus Extract and Its Biomedical Applications. *Crystals* **2022**, *12*, 1142. [CrossRef]
116. Lee, M.; Kim, M.Y.; Kim, J.; Park, C.O.; Choa, H.E.; Lee, S.Y.; Park, M.K.; Min, H.; Lee, K.H.; Lee, W. Conductometric Sensor for Gaseous Sulfur-Mustard Simulant by Gold Nanoparticles Anchored on ZnO Nanosheets Prepared via Microwave Irradiation. *Sens. Actuators B Chem.* **2023**, *386*, 133726. [CrossRef]
117. Yan, P.; Hu, Q.; Chen, J.; Zhou, N.; Zhang, Q. Gas Sensing Property of ZnO NR Arrays Stabilized by High-Temperature Annealing and the Mechanism of Detecting Reduce Gases. *J. Phys. Chem. Solids* **2023**, *181*, 111488. [CrossRef]
118. Findik, M. ZnO Nanoflowers Modified Pencil Graphite Electrode for Voltammetric DNA Detection and Investigation of Gemcitabine–DNA Interaction. *Mater. Chem. Phys.* **2023**, *307*, 128117. [CrossRef]
119. Ahmad, H.; Naderi, N.; Yasin, M. Design and Photovoltaic Performance Analysis of Electrodeposited ZnO Microspheres/p-Si Heterojunction Energy Harvesters. *J. Mater. Sci. Mater. Electron.* **2023**, *34*, 414. [CrossRef]
120. Nakate, U.T.; Yu, Y.-T.; Park, S. Hydrothermal Synthesis of ZnO Nanoflakes Composed of Fine Nanoparticles for H_2S Gas Sensing Application. *Ceram. Int.* **2022**, *48*, 28822–28829. [CrossRef]
121. Manzano, C.V.; Philippe, L.; Serrà, A. Recent Progress in the Electrochemical Deposition of ZnO Nanowires: Synthesis Approaches and Applications. *Crit. Rev. Solid State Mater. Sci.* **2022**, *47*, 772–805. [CrossRef]
122. Sampath, S.; Rohini, V.; Chinnasamy, K.; Ponnusamy, P.; Thangarasau, S.; Kim, W.K.; Shkir, M.; Reddy, V.R.M.; Maiz, F. Solvothermal Synthesis of Magnetically Separable Co–ZnO Nanowires for Visible Light Driven Photocatalytic Applications. *Phys. B Condens. Matter* **2023**, *652*, 414654. [CrossRef]